10-2016

Interseismic Deformation and Moment Deficit Along the Manila Subduction Zone and the Philippine Fault System

Ya-Ju Hsu
Academia Sinica,

Shui-Beih Yu
Academia Sinica

John P. Loveless
Smith College, jloveles@smith.edu

Teresito Bacolcol
Philippine Institute of Volcanology and Seismology,

Renato Solidum
Philippine Institute of Volcanology and Seismology,

See next page for additional authors

AGU PUBLICATIONS

JGR

Journal of Geophysical Research: Solid Earth

RESEARCH ARTICLE
10.1002/2016JB013082

Key Points:
- Inferred coupling ratio is 0.34–0.48 at latitudes 15–19°N along the Manila Trench
- The Manila subduction zone is subject to threats of earthquakes with M_w~9.0
- Inferred Mw of inland large earthquakes in Luzon ranges from 6.9 to 7.6

Supporting Information:
- Supporting Information S1

Correspondence to:
Y.-J. Hsu,
yaru@earth.sinica.edu.tw

Citation:
Hsu, Y.-J., S.-B. Yu, J. P. Loveless, T. Bacolcol, R. Solidum, A. Luis Jr, A. Pelicano, and J. Woessner (2016), Interseismic deformation and moment deficit along the Manila subduction zone and the Philippine Fault system, *J. Geophys. Res. Solid Earth*, *121*, 7639–7665, doi:10.1002/2016JB013082.

Received 12 APR 2016
Accepted 9 OCT 2016
Accepted article online 11 OCT 2016
Published online 30 OCT 2016

Interseismic deformation and moment deficit along the Manila subduction zone and the Philippine Fault system

Ya-Ju Hsu[1], Shui-Beih Yu[1], John P. Loveless[2], Teresito Bacolcol[3], Renato Solidum[3], Artemio Luis Jr[3], Alfie Pelicano[3], and Jochen Woessner[4]

[1]Institute of Earth Sciences, Academia Sinica, Taipei, Taiwan, [2]Department of Geosciences, Smith College, Northampton, Massachusetts, USA, [3]Philippine Institute of Volcanology and Seismology, Quezon City, Philippines, [4]Risk Management Solutions Inc., Zurich, Switzerland

Abstract We examine interseismic coupling of the Manila subduction zone and fault activity in the Luzon area using a block model constrained by GPS data collected from 1998 to 2015. Estimated long-term slip rates along the Manila subduction zone show a gradual southward decrease from 90–100 mm/yr at the northwest tip of Luzon to 65–80 mm/yr at the southern portion of the Manila Trench. We provide two block models (models *A* and *B*) to illustrate possible realizations of coupling along the Manila Trench, which may be used to infer future earthquake rupture scenarios. Model *A* shows a low coupling ratio of 0.34 offshore western Luzon and continuous creeping on the plate interface at latitudes 18–19°N. Model *B* includes the North Luzon Trough Fault and shows prevalent coupling on the plate interface with a coupling ratio of 0.48. Both models fit GPS velocities well, although they have significantly different tectonic implications. The accumulated strain along the Manila subduction zone at latitudes 15–19°N could be balanced by earthquakes with composite magnitudes of M_w 8.8–9.2, assuming recurrence intervals of 500–1000 years. GPS observations are consistent with full locking of the majority of active faults in Luzon to a depth of 20 km. Inferred moments of large inland earthquakes in Luzon fall in the range of M_w 6.9–7.6 assuming a recurrence interval of 100 years.

1. Introduction

The Manila subduction zone is located at the plate boundary where the Sunda Plate (SP) converges obliquely with the Philippine Sea Plate (PSP) at a rate of 83–94 mm/yr [*Sella et al*., 2002; *Kreemer et al*., 2003] (Figure 1a). The convergence rate between SP and PSP is among the highest in the world and is accommodated by two opposite-polarity subduction zones: the east dipping Manila Trench to the west and the west dipping Philippine Trench and the East Luzon Trough to the east [*Fitch*, 1972; *Karig*, 1973]. Subduction along the Manila Trench is hindered in the central Philippines by the collision between the continental Palawan block and Mindoro [*Aurelio*, 2000] (Figure 1a). Due to oblique subduction, accumulated strain is partitioned between the Manila subduction zone and the Philippine Fault (Figure 1), a major sinistral strike-slip fault system extending 1300 km from northern Luzon to Mindanao [*Barrier et al*., 1991; *Aurelio*, 2000].

Historical seismicity over the past century has been characterized by infrequent large earthquakes along the Manila subduction zone (Figure 2a). Luzon was colonized by the Spanish beginning in 1560, and no earthquakes with magnitude larger than 8 have been reported since then [*Megawati et al*., 2009]. Recent seismicity from the Global Centroid Moment Tensor (GCMT) Project between 1976 and 2014 shows a paucity of large earthquakes as well (Figure 2b). Two major earthquakes have occurred in this region, including the 1990 M_s 7.8 Luzon, Philippines earthquake and 2006 M_w 7.2 Pingtung earthquake offshore southern Taiwan. The 1990 earthquake ruptured the left-lateral Philippine Fault and generated a surface rupture more than 100 km long [*Yoshida and Abe*, 1992]. On the other hand, the 2006 Pingtung, Taiwan earthquake is associated with a west dipping normal fault, with a hypocentral depth of 44 km. This earthquake may be associated with the bending of the subducting lithosphere [*Wu et al*., 2009].

Previous studies have used GPS data to estimate fault locking depths and slip rates on major faults in Luzon and on the plate boundary. Due to sparse geodetic coverage in Luzon, *Galgana et al*. [2007] were only able to resolve fault slip rates on two major branches of the Philippine Fault and the Northern Cordillera Fault. *Hsu et al*. [2012] removed the effect of interseismic deformation from the Philippine Fault and solely examined the strain accumulation on the Manila subduction zone. *Yu et al*. [2013] inferred the locking depth and slip-deficit rate on the Philippine Fault using a two-dimensional dislocation model. To gain a comprehensive

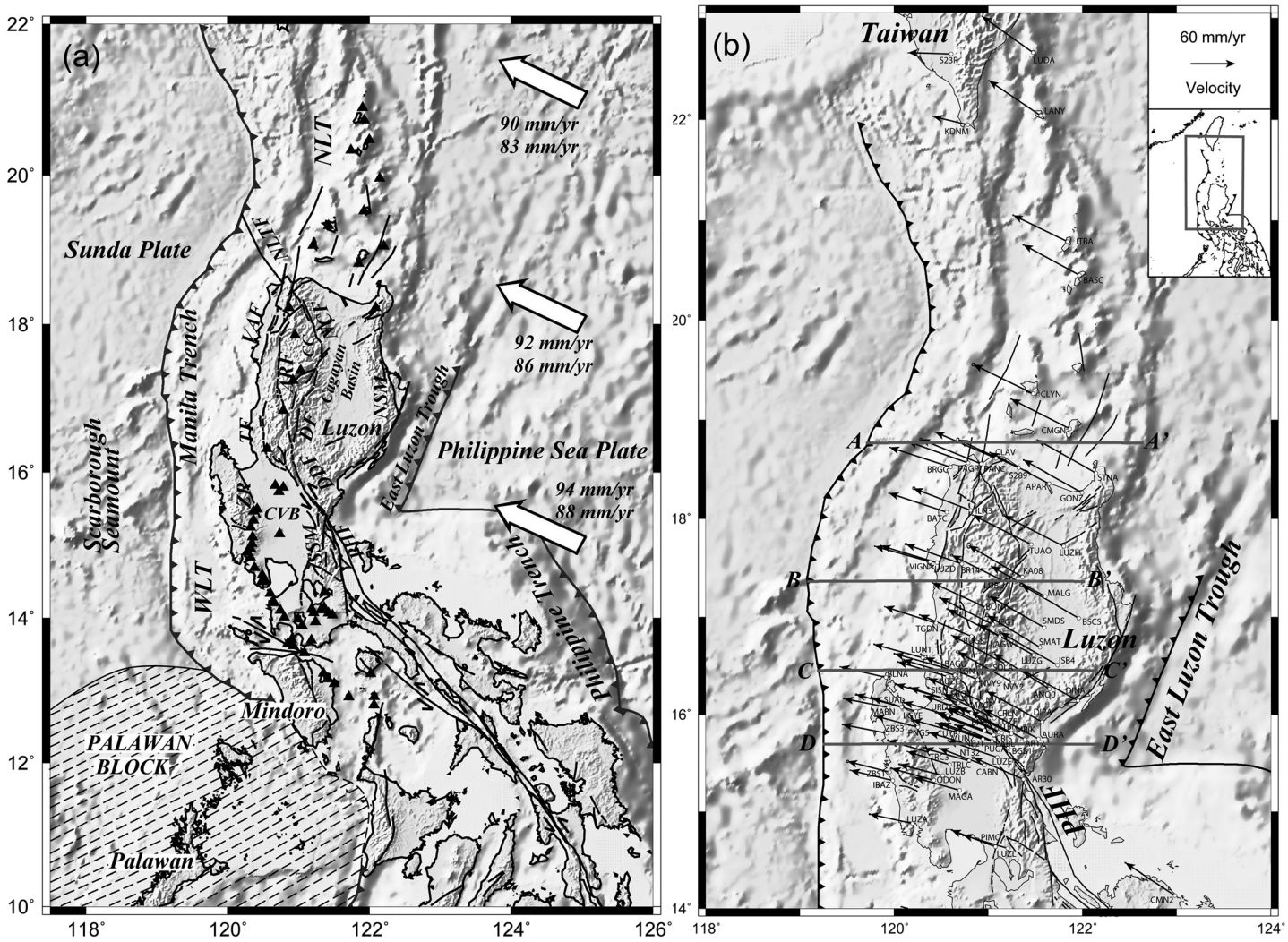

Figure 1. Tectonic setting and GPS velocities in northern Philippines. (a) Convergence between the Sunda Plate and the Philippine Sea Plate is accommodated along the Manila Trench to the west and the Philippine Trench and the East Luzon Trough to the east. The white vectors and black text show the convergence rates estimated from models *A* and *B* at different latitudes. The volcanoes associated with eastward dipping subduction are shown as black triangles. NLTF: North Luzon Trough Fault; ARF: Abra River Fault; CVB: Central Valley Basin; CC: Central Cordillera; DF: Dalton Fault; DDF: Digdig Fault; NCF: Northern Cordillera Fault; NLT: North Luzon Trough; PHF: Philippine Fault; VAF: Vigan-Aggao Fault; WTL: West Luzon Trough; NSM/SSM: Northern/Southern Sierra Madre; ZR: Zambales Range. (b) To characterize regional tectonic motion, we transform ITRF2008 velocities into the Sunda-fixed reference frame [*Simons et al*., 2007]. The station velocities with respect to the Sunda Plate are about 60–90 mm/yr in the west-northwest (WNW) to northwest (NW) directions and gradually decrease from north to south and east to west. The error ellipses indicate the 67% confidence intervals of GPS velocities. The black lines indicate the major active faults. *A*-*A*′ to *D*-*D*′ are four EW trending transects of GPS velocities in Figure 4 with widths of 150, 130, 60, and 110 km, respectively. The inset shows the regional geography and tectonic setting.

understanding of the processes that contribute to observed deformation, we deployed 31 continuous GPS stations (cGPSs) since 2008 and increased the survey-mode station density by a factor of 2 in central and northern Luzon (Figure 1b). The newly collected GPS data allow us to develop a more detailed model taking into account the complex fault systems in Luzon and adjacent subduction zones.

Here we examine interseismic coupling of the Manila subduction zone and the Luzon area using a spherical block model constrained by dense GPS measurements that have been collected since 2008. This method simultaneously estimates microplate (block) rotations and elastic strain accumulation associated with the earthquake cycle. We attempt to assess spatially variable coupling along the Manila Trench and slip-deficit rates on major faults in Luzon. Using geodetically constrained slip rate models, we evaluate the moment accumulation rates and the maximum size of potential future earthquakes on major faults. Additionally, the slip vectors of large earthquakes can provide a complementary view of the relative motion between plate

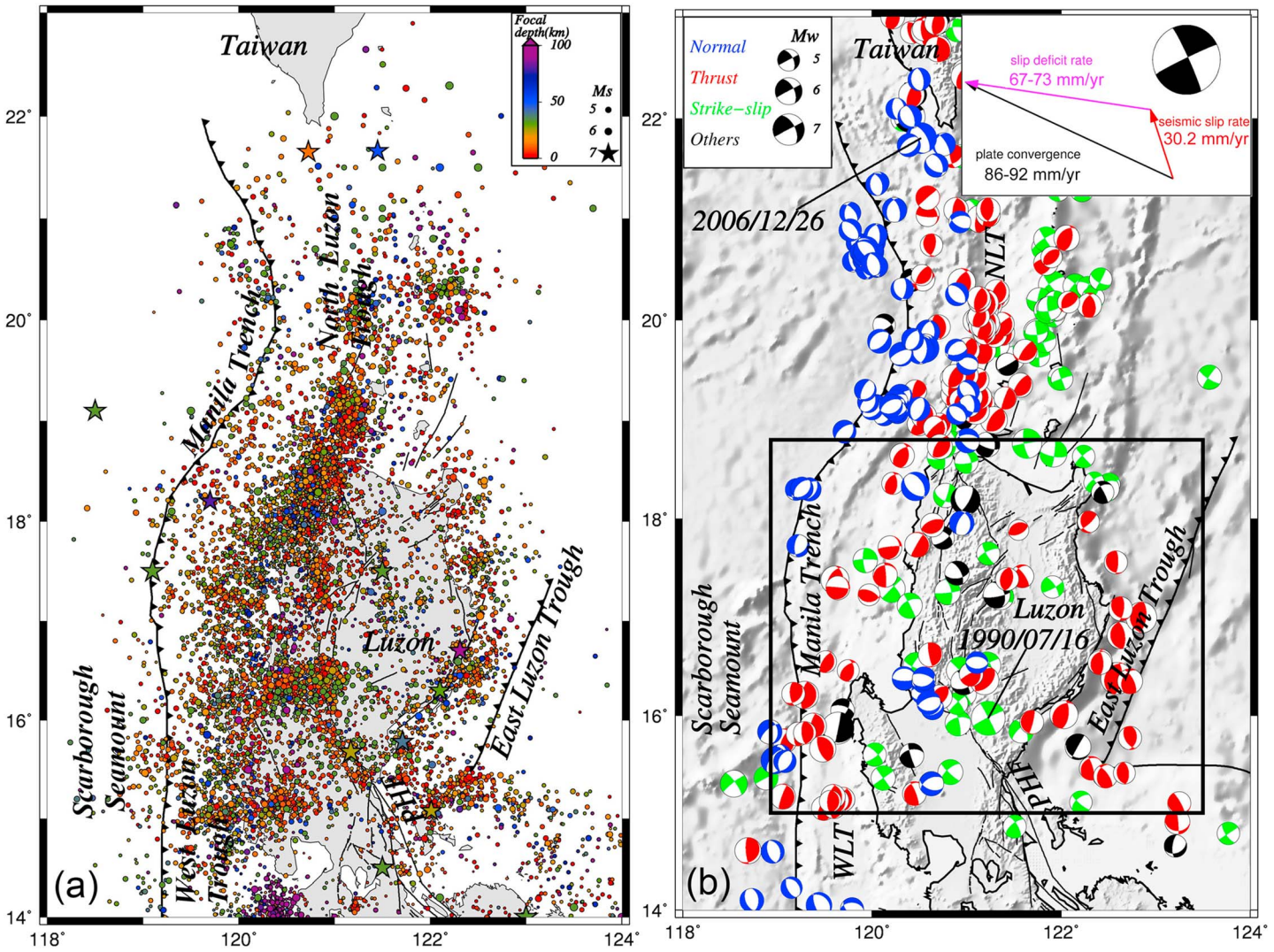

Figure 2. Seismicity in northern Philippines. (a) Seismicity from PHIVOLCS between 1900 and 2014 [*Bautista*, 1996; *Bautista and Oike*, 2000; *Bautista and Bautista*, 2004]. The color indicates the focal depths, and the size of the circle is proportional to the magnitude. (b) Earthquake focal mechanisms with depths shallower than 50 km between 1976 and 2014 from GCMT. The color denotes the different focal mechanism types shown on the top left corner. The box at the top right shows the vector circuit between the plate convergence, slip-deficit, and seismic slip rates. The focal mechanism indicates the composite moment tensor given by the sum of moment tensors in the black box. NLT: North Luzon Trough; WTL: West Luzon Trough; PHF: Philippine Fault.

boundary faults [*Minster and Jordan*, 1978]. We also examine the strain rate tensor from the sum of earthquake moment tensors and compare these values with our block modeling results, with the assumption that slip deficit inferred from seismic strain rate and plate convergence rate is indicative of the strain budget in the plate boundary zone.

2. Tectonic Setting

The Philippines is the product of the Neogene collision between the Sunda Plate (SP) and the Philippine Sea Plate. It is composed of a mosaic of ophiolites, marginal basins, continental fragments, and magmatic arc terranes accreted during Tertiary [*Karig*, 1983; *Barrier et al.*, 1991]. This collision led to the development of two volcanic chains, which are separated by 50 km just north of Luzon (latitudes 18°N) and converge near latitudes 20°N (Figure 1a). The western chain is composed of volcanic rocks of Miocene to Pliocene, whereas the eastern chain is composed of primary Quaternary volcanoes [*Yang et al.*, 1996].

Luzon is primary composed of N-S trending morphostructrural units [*Pinet and Stephan*, 1990; *Ringenbach et al*., 1990]. The NW-SE trending Philippine Fault in central Luzon cuts across N-S trending structures and separates the Central Cordillera, Cagayan Basin, and Northern Sierra Madre to the NE from the Zambales Range, Central Valley Basin, and Southern Sierra Madre to the SW (Figure 1). The Central Cordillera and the Southern Sierra Madre are both formed by an Oligocene-Miocene volcanic-plutonic axis [*Wolfe*, 1981]. The E-W offset of 80–100 km between these two mountain ranges reflects the minimum cumulative left-lateral motion along the Philippine Fault in central Luzon [*Pinet and Stephan*, 1990]. The Central Cordillera, with a height of up to 3000 m, corresponds to the uplift and tectonized magmatic arc associated with the Manila subduction zone [*Ringenbach et al*., 1990]. In northern Luzon, the Cagayan Basin is a north-south trending interarc basin in which 10 km of marine, transitional marine, and fluvial sediments have been deposited since the Oligocene [*Mathisen*, 1981]. The Northern Sierra Madre Mountains are composed primarily of andesitic rocks, with early Tertiary metavolcanic and metasedimentary beds in marginal areas. The Central Valley Basin contains late Eocene to recent sedimentary fill which reaches 14 km thickness in its central part [*Pinet and Stephan*, 1990]. The Zambales Range is composed of Eocene ophiolite, and a much larger Eocene ophiolite basement is likely to extend eastward underneath the Central Valley Basin and into the Southern Sierra Madre.

3. Data

3.1. Geological Data

The active fault map of Philippines (http://www.phivolcs.dost.gov.ph/) compiled by Philippine Institute of Volcanology and Seismology (PHIVOLCS) is used to guide the locations of block-bounding faults considered in the modeling (Figure 1a). Major active faults in the study area include the left-lateral Philippine Fault system, Northern Cordillera Fault, and Vigan-Aggao Fault (Figure 1a). The Vigan-Aggao Fault is located at the boundary between highly deformed Mesozoic ophiolite and a paleo-basin filled with a thick late Eocene to Miocene sedimentary sequence [*Pinet and Stephan*, 1990]. Little is known of the Northern Cordillera Fault due to its inaccessibility.

In Luzon, the Philippine Fault is characterized by a complex braided system of left-lateral strike-slip strands [*Ringenbach et al*., 1993]. The main splays from east to west are the Digdig Fault, Dalton Fault, Abra River Fault, and Tubao Fault. The Digdig Fault ruptured for about 120 km during the M_s 7.8, 16 July 1990 earthquake. The average coseismic left-lateral slip was estimated to be 5.4 m based on a seismic inversion [*Yoshida and Abe*, 1992] and 5.5–6.5 m from a geodetic inversion [*Silcock and Beavan*, 2001]. The Abra River Fault, the main splay of the Philippine Fault in northern Luzon, separates the deformed infill from the strongly uplifted pre-late Miocene basement rocks on the west side from the basement disconformably overlain by the Miocene-Pliocene sequence on the east side [*Ringenbach et al*., 1990]. The left-lateral Pugo Fault and Tebbo Fault bound South Central Cordillera to the west and east, respectively [*Aurelio et al*., 2009]. Except for the Philippine Fault in central Luzon, detailed studies of the long-term slip rates on most faults are hampered by the lack of data and geological complications. Estimates of slip rate on the Digdig Fault segment are 9–17 mm/yr based on geological and paleoseismological data [*Daligdig*, 1997].

3.2. GPS Data

The GPS network in Luzon was established in late 1995 and first measured in 1996 by the Institute of Earth Sciences, Academia Sinica, Taiwan, in collaboration with PHIVOLCS, Philippines [*Yu et al*., 1999]. The network was initially composed of 15 stations, and 16 additional stations were added into the network in central and southern Luzon between 1998 and 1999. Subsequent GPS surveys were done annually until 2000. Three additional campaigns were conducted in 2004, 2006, and 2008. New continuous GPS (cGPS) sites have been constructed since 2008, and the current network is composed of 31 continuous (including an International Global Navigation Satellite Systems Service (IGS) site, PIMO) and 53 survey-mode sites in Luzon (Figure 1b). The typical cGPS site in Luzon is equipped with a dual-frequency geodetic GPS receiver, an antenna, and batteries with charger for backup electric power. The antennas are mounted on stainless steel rods installed on concrete buildings or in bedrock for cGPS stations. We record data with a 30 s sampling rate. For the survey-mode sites, we conduct repeated surveys using a tripod system with calibrated optical plummet and collect data for 2–3 days at each station with a 30 s sampling rate.

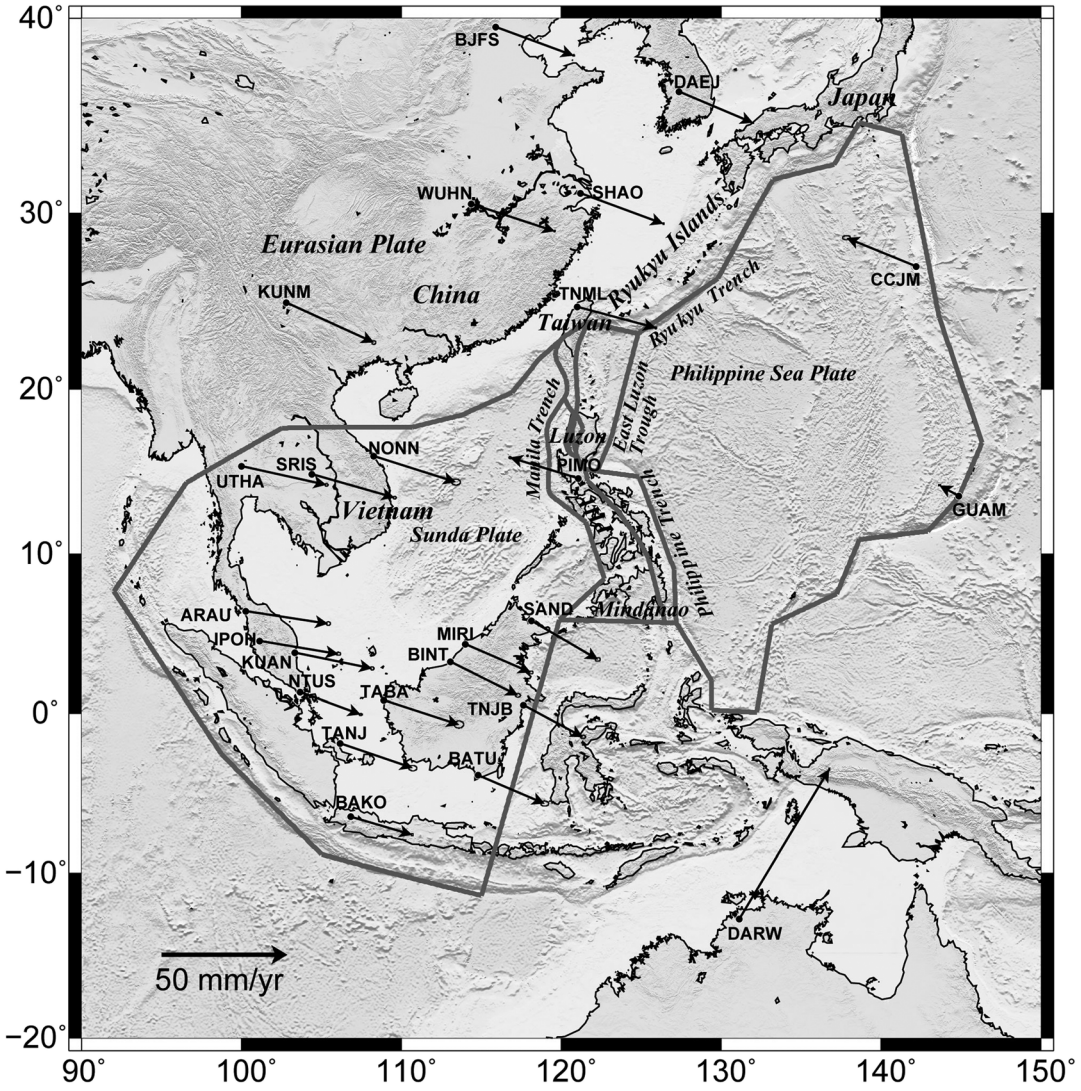

Figure 3. Shaded relief map of Southeast Asia region and major tectonic features. The black dots indicate the IGS sites and cGPS sites in *Simons et al.* [2007] used for this study. The black vectors show the GPS velocities with 67% confidence ellipses in ITRF2008. The gray lines show the block boundaries of model *B*. PHF: Philippine Fault.

The collected GPS data from 1998 to 2015 are processed with the GAMIT 10.42/GLOBK 5.16 software packages [*Herring et al.*, 2002] using the double-differenced ionosphere-free carrier phase observations (L3) as the basic observables. The residual tropospheric zenith delay is estimated every 2 h per station simultaneously with the station coordinates by a least squares adjustment. To obtain a more accurate and consistent regional deformation pattern in Luzon, we use GPS data from 13 International Global Navigation Satellite Systems Service (IGS) sites in the Asia-Pacific region (Figure 3) and 7 sites from Taiwan continuous GPS Array; these observations are incorporated with those from the Luzon sites in the data processing. A well-distributed subset of IGS Reference Frame stations, called the IGb08 core network, is used for alignment of our regional solutions to the IGb08 Reference Frame (IGSMails 6354 and 6663 [*Rebischung et al.*, 2012]).

The velocity of each cGPS site is calculated from the time series of station position through a model by removing outliers and systematic errors. The model includes a linear rate, annual, and semiannual periodic motions and offsets caused by coseismic jumps and instrument changes. The cGPS data used in this study are shown in Figure S1 in the supporting information and Table 1. We also consider noise characteristics in time series of station position as a combination of white noise and flicker noise [*Zhang et al.*, 1997; *Mao et al.*, 1999; *Nikolaidis*, 2002; *Williams*, 2003]. A more realistic noise model can give a better estimate of the full covariance

Table 1. GPS Site Velocity in ITRF2008 Reference Frame

Site	Latitude (°)	Longitude (°)	V_e (mm/yr)	V_n (mm/yr)	V (mm/yr)	Time period (year)
Survey-mode						
ANQ0	16.2603	121.6494	−42.6 ± 1.4	33.5 ± 1.5	54.1 ± 2.1	2008.6~2015.3
AR17	15.7398	121.3888	−41.8 ± 1.2	23.9 ± 0.7	48.1 ± 1.4	2008.6~2015.3
AR30	15.3330	121.3725	−35.1 ± 1.4	15.1 ± 0.9	38.2 ± 1.6	2008.7~2015.3
BGB1	15.6561	121.2144	−39.3 ± 0.6	16.8 ± 0.6	42.7 ± 0.9	2000.3~2015.3
BNBA	15.8337	120.9597	−32.7 ± 1.0	10.7 ± 1.0	34.3 ± 1.4	2008.6~2015.3
BR14	17.5384	120.7185	−42.4 ± 1.0	12.6 ± 0.8	44.3 ± 1.2	2009.8~2015.3
BSCS	16.9865	121.9588	−44.4 ± 1.5	30.1 ± 1.2	53.6 ± 1.9	2009.9~2015.3
CMN2	14.1344	122.9827	−34.7 ± 0.5	29.0 ± 0.4	45.2 ± 0.7	1998.1~2015.3
CMS2	13.7609	123.2861	−31.0 ± 0.7	28.5 ± 0.6	42.1 ± 0.9	1998.1~2011.4
CRIS	15.7829	121.0595	−39.2 ± 0.9	13.1 ± 0.5	41.3 ± 1.0	2000.3~2014.8
CRLN	15.9596	121.0640	−36.3 ± 1.2	18.8 ± 0.8	40.8 ± 1.4	2008.6~2015.3
CUYP	15.8121	120.6775	−28.7 ± 1.3	3.3 ± 1.5	28.9 ± 1.9	2009.8~2015.3
DINA	16.1397	121.9524	−44.5 ± 1.3	27.6 ± 1.0	52.4 ± 1.6	2008.6~2015.3
DIPA	15.9226	121.5739	−42.5 ± 0.9	26.9 ± 1.1	50.3 ± 1.4	2008.6~2015.3
IFG1	16.9206	121.0515	−38.8 ± 0.7	21.6 ± 0.5	44.4 ± 0.9	1998.4~2015.3
ILN3	18.0846	120.8147	−43.8 ± 1.2	15.5 ± 1.3	46.5 ± 1.8	2009.8~2015.3
ISB4	16.5036	121.7370	−44.5 ± 1.0	29.9 ± 1.0	53.6 ± 1.4	2008.6~2015.3
ITGN	16.4004	120.6462	−37.2 ± 0.9	6.8 ± 0.9	37.8 ± 1.2	2008.7~2015.3
KA08	17.4035	121.3648	−39.8 ± 1.5	28.4 ± 2.5	48.9 ± 2.9	2009.8~2015.3
LUBU	17.3550	121.1789	−39.1 ± 1.0	21.6 ± 0.8	44.7 ± 1.3	2010.3~2015.3
LUN1	16.5826	120.3044	−32.7 ± 0.6	4.1 ± 0.5	33.0 ± 0.7	1998.4~2012.1
LUZA	14.8775	120.1953	−25.4 ± 0.5	−1.2 ± 0.6	25.4 ± 0.8	1998.1~2015.3
LUZB	15.3728	120.5171	−26.3 ± 0.6	1.2 ± 0.6	26.3 ± 0.9	1998.1~2009.8
LUZC	16.3880	120.5682	−34.1 ± 0.5	5.9 ± 0.5	34.6 ± 0.7	1998.1~2015.3
LUZD	17.5509	120.4556	−42.6 ± 0.6	8.9 ± 0.4	43.5 ± 0.7	1998.1~2015.3
LUZE	15.5610	121.0970	−34.1 ± 0.6	8.2 ± 0.5	35.1 ± 0.8	1998.1~2015.3
LUZF	15.8136	121.1131	−39.0 ± 0.5	18.0 ± 0.4	42.9 ± 0.7	1998.1~2015.3
LUZG	16.6075	121.4821	−41.5 ± 0.8	27.2 ± 0.5	49.6 ± 0.9	1998.1~2015.3
LUZH	17.7174	121.8038	−48.6 ± 0.9	27.5 ± 0.7	55.8 ± 1.1	1998.1~2015.3
LUZL	14.6201	121.2080	−27.7 ± 0.8	3.5 ± 0.7	27.9 ± 1.1	1998.1~2006.9
LUZP	13.8145	120.9753	−14.6 ± 0.9	−2.9 ± 0.8	14.9 ± 1.2	1998.1~2012.1
MACR	16.0107	120.8201	−30.6 ± 0.9	9.5 ± 0.8	32.0 ± 1.2	1998.1~2012.1
MAGA	15.2200	120.6957	−28.1 ± 0.9	3.2 ± 0.7	28.2 ± 1.1	2006.9~2015.3
MRIK	15.7998	121.2483	−39.8 ± 0.9	21.9 ± 0.9	45.4 ± 1.3	2008.6~2015.3
N132	15.5244	120.7974	−28.0 ± 1.0	2.9 ± 0.9	28.2 ± 1.3	2008.6~2014.3
NE21	15.6717	120.8535	−28.1 ± 1.1	4.0 ± 0.6	28.4 ± 1.2	2008.6~2014.3
NVY2	16.3273	121.2611	−41.5 ± 1.4	27.0 ± 1.0	49.5 ± 1.7	2008.6~2015.3
NVY3	16.1329	120.9300	−39.4 ± 1.4	17.1 ± 0.9	42.9 ± 1.7	2008.6~2015.3
NVY9	16.3580	120.8883	−37.8 ± 1.5	15.8 ± 1.9	40.9 ± 2.4	2008.6~2015.3
ODON	15.3241	120.4232	−25.1 ± 0.9	2.1 ± 0.7	25.2 ± 1.1	2008.7~2015.3
PABL	15.7856	121.0615	−36.5 ± 0.6	13.4 ± 0.7	38.9 ± 0.9	2000.3~2014.8
PANC	18.5508	120.9271	−48.7 ± 1.0	19.3 ± 1.1	52.4 ± 1.5	2009.8~2014.3
PNG5	15.8677	120.2537	−25.2 ± 0.9	1.5 ± 0.6	25.2 ± 1.1	2008.6~2014.3
PUGA	15.7261	121.0407	−35.5 ± 0.9	10.1 ± 0.7	36.8 ± 1.2	2000.3~2011.1
S289	18.5137	121.3218	−48.8 ± 1.2	23.7 ± 1.5	54.3 ± 1.9	2009.8~2013.0
SISN	16.1626	120.5152	−30.7 ± 0.8	5.2 ± 0.7	31.1 ± 1.1	2008.7~2015.3
SMAT	16.6862	121.5510	−38.8 ± 1.6	29.0 ± 1.3	48.4 ± 2.1	2009.8~2015.3
SMDS	16.8902	121.5983	−41.4 ± 1.4	27.7 ± 1.2	49.8 ± 1.9	2009.9~2015.3
SRQE	16.1178	120.6813	−32.6 ± 1.4	6.6 ± 0.6	33.3 ± 1.5	2009.8~2015.3
SUAL	16.0724	120.0809	−28.7 ± 0.9	3.4 ± 0.7	28.9 ± 1.1	2006.9~2015.3
TRC3	15.6095	120.3838	−24.5 ± 0.6	2.4 ± 0.7	24.6 ± 1.0	2008.6~2015.3
ZBS1	15.4092	119.9525	−23.9 ± 0.9	0.6 ± 1.1	23.9 ± 1.4	2008.7~2015.3
ZBS3	15.8057	119.9247	−27.0 ± 0.7	−2.0 ± 0.6	27.0 ± 0.9	1998.3~2015.3
cGPS						
APAR	18.3553	121.6473	−46.8 ± 0.5	27.3 ± 0.4	54.2 ± 0.6	2010.3~2014.9
AURA	15.7471	121.5324	−41.8 ± 0.4	25.6 ± 0.2	49.0 ± 0.4	2008.9~2015.3
BAGU	16.4611	120.5885	−41.8 ± 0.4	7.2 ± 0.6	42.4 ± 0.8	2008.9~2013.9
BASC	20.4501	121.9695	−42.5 ± 0.5	26.7 ± 0.5	50.1 ± 0.7	2011.8~2015.4
BATC	18.0636	120.5596	−45.1 ± 0.5	11.9 ± 0.3	46.6 ± 0.5	2010.3~2015.1
BLNA	16.3787	119.9147	−29.2 ± 0.3	0.7 ± 0.3	29.2 ± 0.4	2010.3~2015.3

Table 1. (continued)

Site	Latitude (°)	Longitude (°)	V_e (mm/yr)	V_n (mm/yr)	V (mm/yr)	Time period (year)
BONT	17.0908	120.9779	−39.7 ± 0.3	19.4 ± 0.3	44.2 ± 0.5	2010.3~2015.3
BRGC	18.5203	120.6007	−48.8 ± 0.3	12.6 ± 0.2	50.4 ± 0.4	2010.3~2015.3
BUGS	16.8001	120.8221	−37.1 ± 0.4	15.0 ± 0.3	40.0 ± 0.5	2011.1~2015.3
CABN	15.4796	120.9602	−28.6 ± 0.2	9.0 ± 0.2	29.9 ± 0.3	2008.9~2014.8
CLAV	18.6069	121.0839	−49.1 ± 0.4	21.4 ± 0.4	53.5 ± 0.5	2011.1~2015.3
CLYN	19.2618	121.4752	−47.4 ± 1.4	25.2 ± 1.4	53.6 ± 1.9	2011.8~2014.8
CMGN	18.9071	121.8673	−46.2 ± 0.5	25.9 ± 0.5	53.0 ± 0.7	2011.8~2015.3
GONZ	18.2612	121.9969	−46.0 ± 0.4	29.5 ± 0.5	54.6 ± 0.7	2010.3~2013.9
IBAZ	15.3218	119.9851	−24.5 ± 0.5	0.0 ± 0.4	24.5 ± 0.6	2012.1~2015.3
ITBA	20.7879	121.8418	−39.9 ± 0.4	21.2 ± 0.5	45.2 ± 0.6	2011.8~2015.4
KDNM	21.9494	120.7820	−13.2 ± 0.2	−2.8 ± 0.2	13.5 ± 0.3	2008.9~2015.4
LAGW	16.7974	121.1229	−38.2 ± 0.7	23.1 ± 0.6	44.7 ± 0.9	2011.1~2014.6
LANY	22.0373	121.5581	−36.2 ± 0.4	33.0 ± 0.4	49.0 ± 0.6	2008.9~2015.3
LGYE	16.0326	120.2345	−26.7 ± 0.5	4.0 ± 0.8	27.0 ± 0.9	2013.0~2015.3
LUDA	22.6581	121.4759	−35.4 ± 0.3	34.8 ± 0.3	49.6 ± 0.4	2007.0~2014.0
MABN	16.0692	119.9406	−27.4 ± 0.5	−1.7 ± 0.5	27.5 ± 0.7	2012.7~2015.3
MALG	17.2051	121.6068	−40.3 ± 0.3	26.5 ± 0.3	48.2 ± 0.4	2010.3~2014.5
MUNZ	15.7442	120.9430	−30.8 ± 0.3	7.9 ± 0.3	31.8 ± 0.4	2011.2~2015.3
PAGP	18.5597	120.7875	−48.4 ± 0.7	15.1 ± 0.7	50.7 ± 1.0	2011.5~2015.3
PPPC	9.7729	118.7402	28.2 ± 0.7	−11.6 ± 0.6	30.5 ± 0.9	2011.0~2014.4
PTBN	15.8081	121.1432	−36.2 ± 0.5	19.5 ± 0.5	41.1 ± 0.7	2011.1~2015.2
S01R	23.6553	119.5924	32.4 ± 0.2	−11.3 ± 0.2	34.3 ± 0.3	2008.9~2015.4
S23R	22.6450	120.6062	−24.2 ± 0.2	−12.3 ± 0.2	27.1 ± 0.3	2008.9~2015.4
SOLA	16.5183	121.1819	−40.0 ± 0.3	24.6 ± 0.2	46.9 ± 0.4	2008.9~2013.3
STNA	18.4575	122.1428	−46.2 ± 0.4	30.5 ± 0.3	55.4 ± 0.5	2011.8~2015.3
TGDN	16.9341	120.4454	−36.4 ± 0.3	8.3 ± 0.2	37.3 ± 0.3	2010.3~2015.3
TNSM	20.7026	116.7246	32.2 ± 0.3	−11.4 ± 0.3	34.1 ± 0.4	2008.8~2013.6
TRLC	15.4863	120.5892	−24.3 ± 0.4	3.5 ± 0.3	24.6 ± 0.5	2008.9~2013.9
TUAO	17.7350	121.4552	−45.7 ± 0.7	25.4 ± 0.3	52.3 ± 0.8	2011.1~2015.3
URDT	15.9889	120.5740	−27.5 ± 0.4	4.0 ± 0.3	27.8 ± 0.5	2011.1~2015.3
VIGN	17.5604	120.3834	−41.7 ± 0.5	7.0 ± 0.4	42.3 ± 0.7	2012.1~2015.3
IGS						
BAKO	−6.4911	106.8489	24.3 ± 0.3	−7.2 ± 0.3	25.3 ± 0.4	2008.9~2011.2
BJFS	39.6086	115.8925	31.0 ± 0.3	−11.5 ± 0.2	33.1 ± 0.4	2008.9~2015.4
CCJM	27.0956	142.1846	−27.6 ± 1.0	11.3 ± 0.6	29.8 ± 1.2	2008.9~2015.4
DAEJ	36.3994	127.3745	29.4 ± 0.2	−12.4 ± 0.1	31.9 ± 0.2	2008.9~2015.4
DARW	−12.8437	131.1327	35.8 ± 0.2	59.6 ± 0.3	69.5 ± 0.4	2008.9~2015.4
GUAM	13.5893	144.8684	−7.7 ± 0.3	4.1 ± 0.2	8.7 ± 0.3	2008.9~2014.4
IRKT	52.2190	104.3162	26.3 ± 0.5	−7.3 ± 0.3	27.3 ± 0.6	2008.9~2014.1
KUNM	25.0295	102.7972	34.8 ± 0.5	−15.9 ± 0.5	38.3 ± 0.7	2008.9~2015.4
NTUS	1.3458	103.6800	24.0 ± 0.5	−8.9 ± 0.2	25.6 ± 0.5	2008.9~2015.4
PIMO	14.6357	121.0777	−27.2 ± 0.3	8.3 ± 0.3	28.4 ± 0.4	2008.9~2015.4
SHAO	31.0996	121.2004	33.0 ± 0.2	−12.2 ± 0.2	35.2 ± 0.3	2008.9~2015.4
TNML	24.7980	120.9873	31.3 ± 0.2	−8.4 ± 0.3	32.4 ± 0.3	2008.9~2015.3
WUHN	30.5317	114.3573	33.2 ± 0.2	−11.0 ± 0.2	35.0 ± 0.3	2008.9~2013.1
***Simons et al.* [2007]**						
ARAU	6.4500	100.2800	32.7 ± 0.6	−5.0 ± 0.5	33.1 ± 0.7	
BATU	−3.8670	114.7910	26.5 ± 1.1	−11.4 ± 0.7	28.9 ± 1.3	
BINT	3.2620	113.0670	26.8 ± 0.7	−13.4 ± 0.5	30.0 ± 0.9	
IPOH	4.5880	101.1260	31.4 ± 0.6	−5.3 ± 0.4	31.8 ± 0.7	
KUAN	3.8340	103.3500	30.7 ± 0.5	−6.3 ± 0.4	31.3 ± 0.7	
MIRI	4.3720	114.0020	26.1 ± 0.6	−11.4 ± 0.4	28.5 ± 0.7	
NONN	16.0040	108.2630	32.7 ± 1.2	−10.4 ± 0.8	34.3 ± 1.4	
SAND	5.8420	118.1210	26.4 ± 0.7	−15.5 ± 0.5	30.6 ± 0.8	
SRIS	14.9010	104.4160	32.8 ± 0.5	−9.4 ± 0.3	34.1 ± 0.6	
TABA	0.8630	108.8910	29.9 ± 1.3	−9.8 ± 1.0	31.5 ± 1.6	
TANJ	−1.8810	106.1760	28.8 ± 1.1	−9.8 ± 0.7	30.4 ± 1.3	
TNJB	0.5580	117.6410	23.7 ± 0.7	−12.8 ± 0.4	26.9 ± 0.8	
UTHA	15.3840	100.0130	33.7 ± 0.4	−7.5 ± 0.3	34.5 ± 0.5	

matrix and model parameters in GPS position time series. The survey-mode GPS data have fewer data points and do not warrant sophisticated analyses. We use a least squares linear fit to estimate station velocities from position time series of survey-mode sites. The velocities, expressed in the International Terrestrial Reference Frame 2008 (ITRF2008) [*Altamimi et al*., 2011], are listed in Table 1. Due to insufficient data north of latitude 19.5°N, we choose to study deformation predominately in Luzon and adjacent offshore areas (Figure 2b).

Additionally, we try to better constrain the motion of the Sunda Plate and select 13 cGPS sites (Figure 3) located outside the deforming region of the Sunda Plate from *Simons et al*. [2007] according to the results in Global Strain Rate Map Project (http://gsrm.unavco.org/model/). The GPS velocities from *Simons et al*. [2007] are converted into the ITRF2008 reference frame and are used together with our data for block modeling (Table 1).

To better visualize the spatial gradient of GPS velocities, we show GPS velocity components in four EW trending transects from north to south (*A*-*A*′ to *D*-*D*′; Figure 1b). The E-W velocity components show a slight eastward increase of about 3 mm/yr on the profile *A*-*A*′ but an eastward decrease increase farther south, from −5 mm/yr on the profile *B*-*B*′ to −20 mm/yr on the *D*-*D*′ (Figure 4). An eastward increase of the N-S velocity component is found at all transects. The differential northward motion at sites located on each side of Luzon increases from 20 mm/yr on the transect *A*-*A*′ to 30 mm/yr on the transect *D*-*D*′. Vertical velocities are mostly within ±5 mm/yr, except for a few sites showing large subsidence due to groundwater withdrawal (Figures 4 and S1). In addition, we examine whether any slow slip events emerge from cGPS daily position time series at sites along the Manila subduction zone (Figures S1 and S2) but find no significant signal, perhaps due to the lack of cGPS sites near the trench axis, long duration of aseismic transients, or infrequent slow slip events on the plate interface fault.

3.3. Earthquake Data

We use earthquake moment tensor solutions determined by GCMT from 1976 to 2014 to study the seismogenic behavior in this region (Figure 2b). Abundant normal-faulting events have occurred near trench axis between the southern tip of Taiwan and northern Luzon. We find a cluster of thrust-faulting earthquakes near the North Luzon Trough and a few thrust events near the Scarborough Seamount that are possibly associated with subducted seafloor roughness [*Hsu et al*., 2012; *Wang and Bilek*, 2014]. Several thrust-faulting earthquakes occurred near the East Luzon Trough, suggesting that this structure is seismically active. Strike-slip faulting events predominately occur adjacent to the Philippine Fault in central Luzon and to the east of the North Luzon Trough. Here we use a total of 126 events (Figure 2b, black box) to calculate the summed moment tensor.

We also use an earthquake catalog from PHIVOLCS covering the period of 1900–2014 (Figure 2a). Detailed description of the methodology in determining the location and magnitude of historical earthquakes can be found in earlier studies [*Bautista*, 1996; *Bautista and Oike*, 2000; *Bautista and Bautista*, 2004]. The PHIVOLCS catalog contains a mixture of local magnitudes (M_L), body wave magnitudes (M_b), and surface wave magnitudes (M_s) ranging from 0 to 8.3 between latitudes 12°N and 20°N. Despite the inclusion of historical events, which could introduce inaccurate locations and magnitudes, a longer record of earthquake history provides in general a better estimate of earthquake recurrence intervals as described in section 6.3. Earthquakes from GCMT and PHIVOLCS catalogs show consistency in spatial distribution (Figure 2). In addition, *Bautista et al*. [2001] inferred a slab tear near latitudes 17–18°N as evidenced by the observed gap in strain energy release at depths of 65–300 km and the abrupt change in slab dip from shallow to steep seen in seismicity (Figure S3). Intermediate depth earthquakes occur again south of latitude 16°N and deep seismicity can be found between 14°N and 15°N [*Bautista et al*., 2001] (Figures 2a and S3).

4. Methods

4.1. Block Modeling

Linear spherical block theory is a method for decomposing the crustal motion into contributions from the rotation of multiple crustal blocks (microplates), homogeneous intrablock strain, and elastic deformation due to fault slip at block boundaries [*McCaffrey*, 2002; *Wallace et al*., 2007; *Meade and Loveless*, 2009a; *Loveless and Meade*, 2010]. We use the observed GPS velocity field and a specified block geometry to simultaneously estimate the rotation vectors of crustal blocks and slip-deficit rates on the Manila Trench, which we

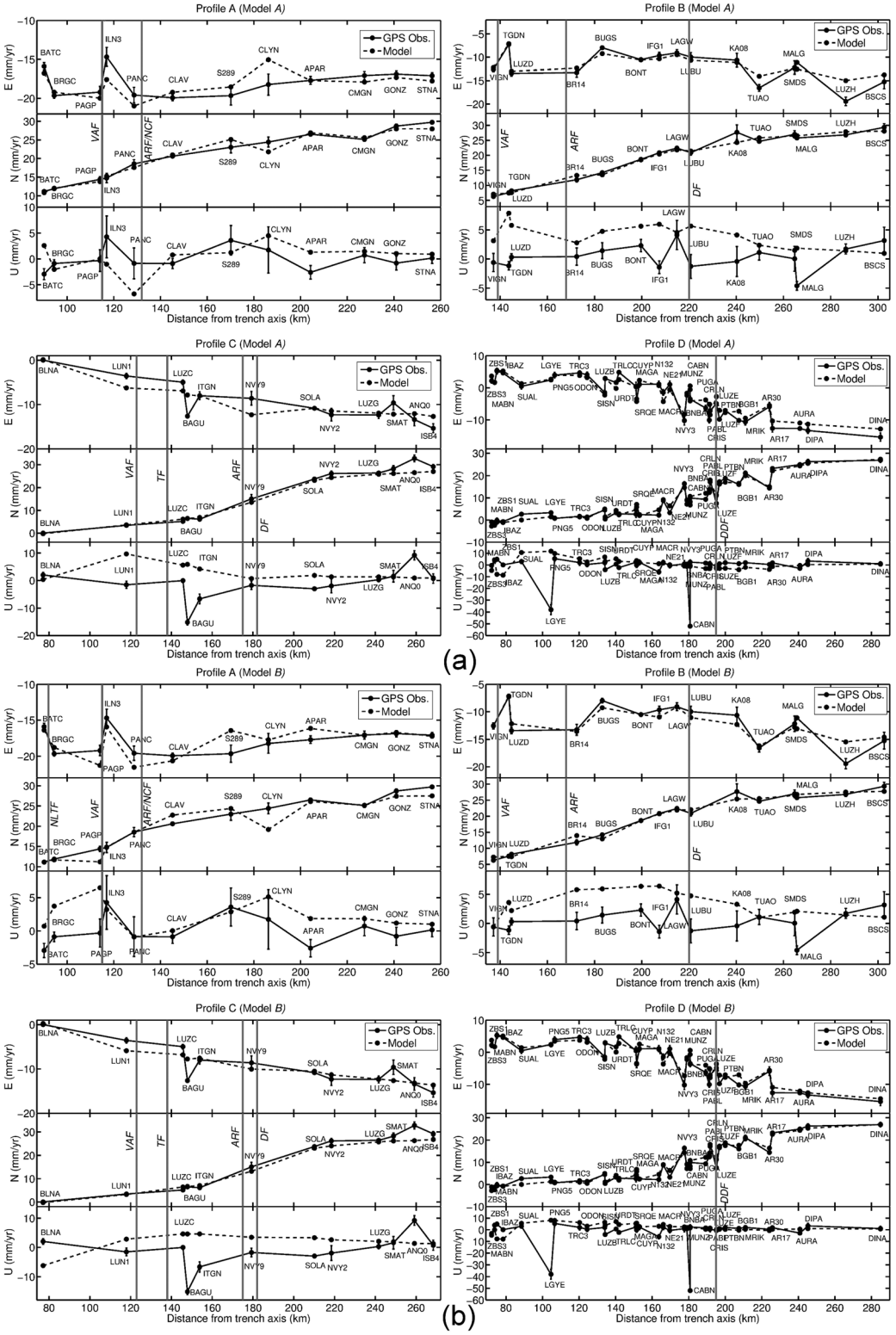

Figure 4. GPS velocity transects in Luzon. EW trending transects of observed GPS (solid lines) and predicted (dash lines) velocities from *A-A'* to *D-D'* (Figure 1b) with widths of 150, 130, 60, and 110 km, respectively. Three plots from top to bottom show the east, north, and vertical components of GPS velocities. Note that GPS vertical velocities are not used in the block modeling. (a) Results from model *A*. (b) Results from model *B*. The black italic texts indicate the fault names. VAF: Vigan-Aggao Fault; NCF: Northern Cordillera Fault; ARF: Abra River Fault; DF: Dalton Fault; TF: Tubao Fault; DDF: Digdig Fault; NLTF: North Luzon Trough Fault.

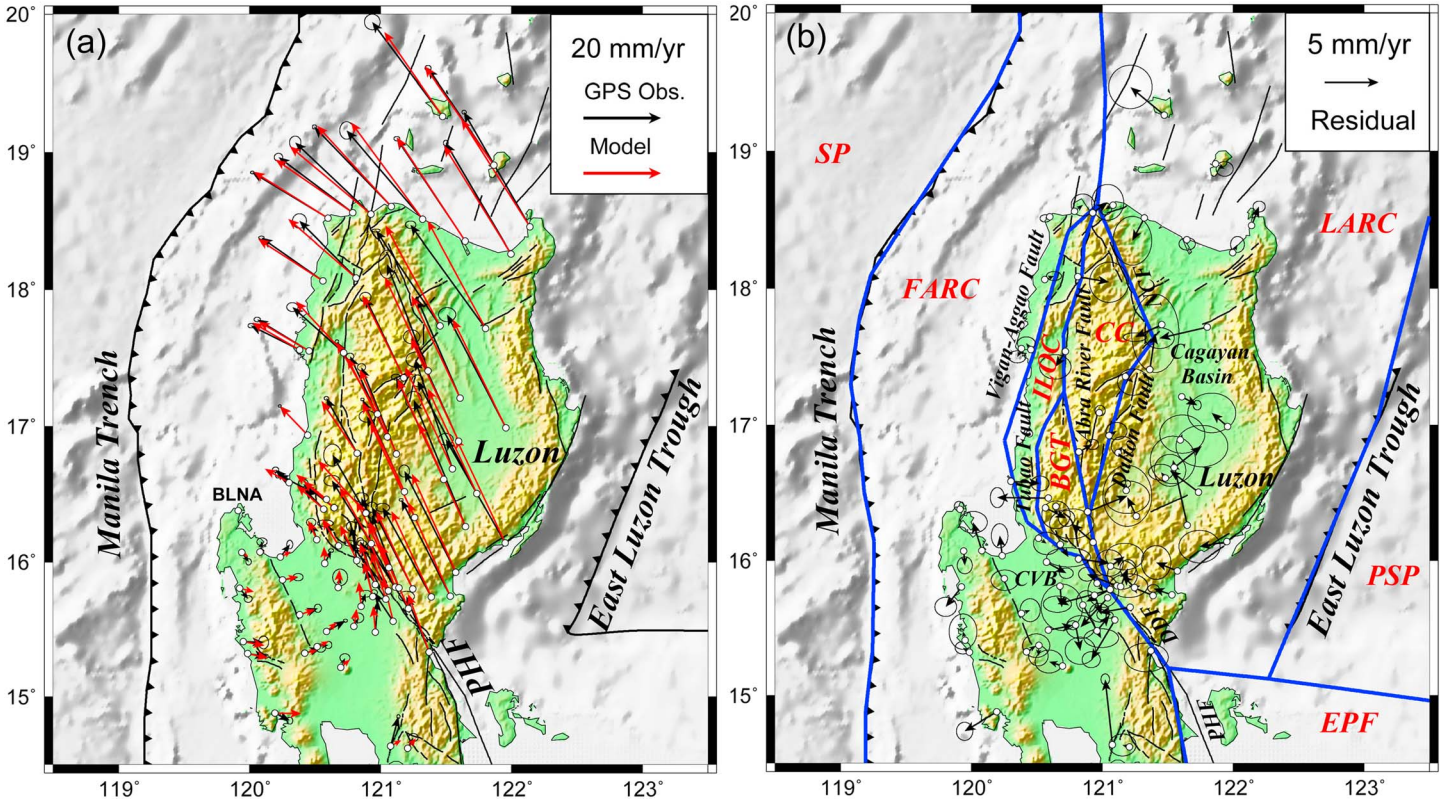

Figure 5. GPS-observed and model-predicted velocities with respect to BLNA in model *A*. (a) The black and red vectors show the observed and predicted velocities, respectively. The error ellipses indicate the 67% confidence intervals of the observed GPS velocities. The black lines indicate the major active faults. (b) Residual velocities are shown in black vectors with 67% confidence ellipses. The blue lines show the block boundaries of model *A*. The red texts indicate the block names (Table 2). PHF: Philippine Fault; DDF: Digdig Fault; NCF: Northern Cordillera Fault; CVB: Central Valley Basin; CC: Central Cordillera.

represent with a continuous mesh of triangular dislocation elements (TDEs). We do not consider intrablock strain because the blocks in Luzon are sufficiently small that estimation of internal strain does not provide a substantially improved fit to GPS data. Long-term fault slip rates are given by projecting relative rotation rates of adjacent blocks onto the bounding fault geometries. We assume that block-bounding faults are fully coupled down to a prescribed locking depth, so that the slip-deficit rate is equal to the long-term slip rate. On the Manila Trench TDEs, we define the spatially variable fault coupling ratio, c, as slip-deficit rate normalized by long-term slip rate. A value of $c = 0$ suggests that the TDE is creeping and $c = 1$ means that the fault is fully coupled. A negative value of c implies that fault slip is faster than the plate convergence rate, which could be interpreted as an ongoing or long-term aseismic transient.

We define a number of tectonic blocks guided by the plate boundary geometry, the active fault map of the Philippines from PHIVOLCS (http://www.phivolcs.dost.gov.ph/), GPS data, seismicity, bathymetry, and topography (Figures 3 and 5). Plate boundary faults include the Manila Trench, the East Luzon Trough, and the Philippine Trench. The geometry of the Manila subduction zone is constrained by the seismicity from 1973 to 2014 at the Bulletin of the International Seismological Center and the trace of the Manila Trench on the seafloor (Figure S4). The slab dips 10°–20° on northern section of the Manila subduction zone and steepens to 20°–50° near Mindoro, where the subduction process ceases. Bending of the slab near latitudes 17–18°N and latitudes 15°N is related to a slab tear suggested in *Bautista et al*. [2001] and by the pattern of seismicity (Figure S3). The Manila megathrust extends to a depth of 70 km, and about 95% of earthquake focal depths are shallower than this depth. Due to a complex slab geometry, we use a single continuous mesh constructed of TDEs to represent the Manila subduction zone and estimate variable slip-deficit rates on the subduction fault. In one variant of the model, we also consider a fault, North Luzon Trough Fault (NLTF), cut through the NLT and connected from the NW tip of Luzon to trench axis as illustrated from the bathymetry (Figure 1a). This fault could be the extension of the Philippine Fault [*Armada et al*., 2012] or accommodates

the deformation due to the bending of the Manila Trench and/or offsets of the fore-arc basins (Figure 1a). The NLTF, East Luzon Trough, and the Philippine subduction zone are modeled using rectangular fault patches, each with a single estimated slip rate.

Major crustal faults in the study area include the left-lateral Philippine Fault system, Northern Cordillera Fault, and Vigan-Aggao Fault [*Pinet*, 1990] (Figure 1a). In Luzon, we consider the Digdig, Dalton, Abra River, Tebbo, Tubao, and Pugo Faults as splays of the Philippine Fault system. Given small distances between the Tebbo and Pugo Faults, and insufficient GPS observations, we represent these closely spaced, subparallel faults with a single trace, the Tubao Fault, to characterize the cumulative deformation across these structures. A tight constraint is imposed for the slip rate on the Digdig Fault to be consistent with the long-term geological slip rate (~15 mm/yr).

We use ITRF2008 velocities to estimate block motions and TDE slip-deficit rates by minimizing residuals between observed and predicted velocities, while simultaneously applying a spatial smoothing constraint on the TDE slip deficits. We impose a zero slip-deficit (creeping) on the deep extent of the Manila subduction zone and full coupling on the lateral extents of the triangular mesh (north of latitude 20°N and south of latitude 14°N). The rationale for full coupling on the lateral extents is that the rectangular segments of the subduction zone adjacent to the meshed region are inherently presumed to be fully coupled, and it is reasonable to introduce a smooth transition from the rectangular segments to the triangular mesh. We test multiple block geometries by adjusting the parameters of major bounding faults constrained by geological data. We vary locking depths from 10 to 25 km on the Philippine Fault system and find that a depth of 20 km gives the minimum residual GPS velocity. Since the locking depth and dip are not well constrained by geological data on the east dipping Vigan-Aggao Fault, we search a wide range of fault parameters to find the optimal solution. Estimates of dip and locking depth are 60° and 20 km, respectively, on the Vigan-Aggao Fault.

At the same time, we test a range of weights applied to the spatial smoothing constraint on the Manila subduction interface, seeking solutions that minimize negative slip deficit (suggesting persistent aseismic slip), and show a good alignment between the rake of slip-deficit and the long-term plate motion in strongly coupled regions. We impose a spatially variable smoothing constraint, inversely proportional to the spatial resolution of slip deficit on the Manila Trench. We calculate this resolution by summing the magnitude of the partial derivatives that relate unit slip on the triangular elements to the displacement at the surface (Figure 6a) [*Loveless and Meade*, 2011]. In general, the spatial resolution is highest beneath the coastline and lowest for triangular fault patches near trench axis. The relation between the average GPS velocity misfit and strength of the smoothness constraint on the plate interface is shown in Figure S5. It appears that there is less trade-off between the prescribed strength of the smoothing constraint and the average misfit because of the full-coupling constraints we impose on the north and south edges of the triangular mesh, although we find broad consistency in results from models without the full-coupling constraints on the lateral extent of the Manila Trench. We choose a smoothing value of 1600 in model *A*. Plate coupling patterns with different smoothing values can be found in Figure S6.

We estimate creep on the Manila subduction interface offshore the NW tip of Luzon shown in model *A* (Figure 6). To produce an alternative model with dominantly thrust-sense slip deficit on the Manila subduction zone, suggesting coupling rather than persistent creeping as shown in model *A*, we segment the subduction zone by introducing the North Luzon Trough Fault from the NW tip of Luzon to trench axis as illustrated from the bathymetry (Figure 1a) and marine geophysical data [*Armada et al*., 2012]. By adding this fault in the block modeling, the normal-sense slip deficit becomes subtle on the Manila subduction zone and the plate interface is about 50% coupled. We use a similar approach as used for model *A* to choose smoothing parameters. The preferred model with a smoothing value of 1600 is named as model *B*. Both models fit GPS velocities well but have significantly different tectonic implications. Given insufficient cGPS and marine geophysical data offshore northern Luzon, we present results from both models and discuss how assumed fault geometries of block models affect the tectonic interpretation.

4.2. Relative Block Motion From Moment Tensors

We adopt the approach proposed by *Ekström and England* [1989] for estimating the relative motion between two deforming regions based on the summation of earthquake moment tensors. Our goal is to compare the rates and configurations of seismic deformation determined from earthquake moment tensors with the plate

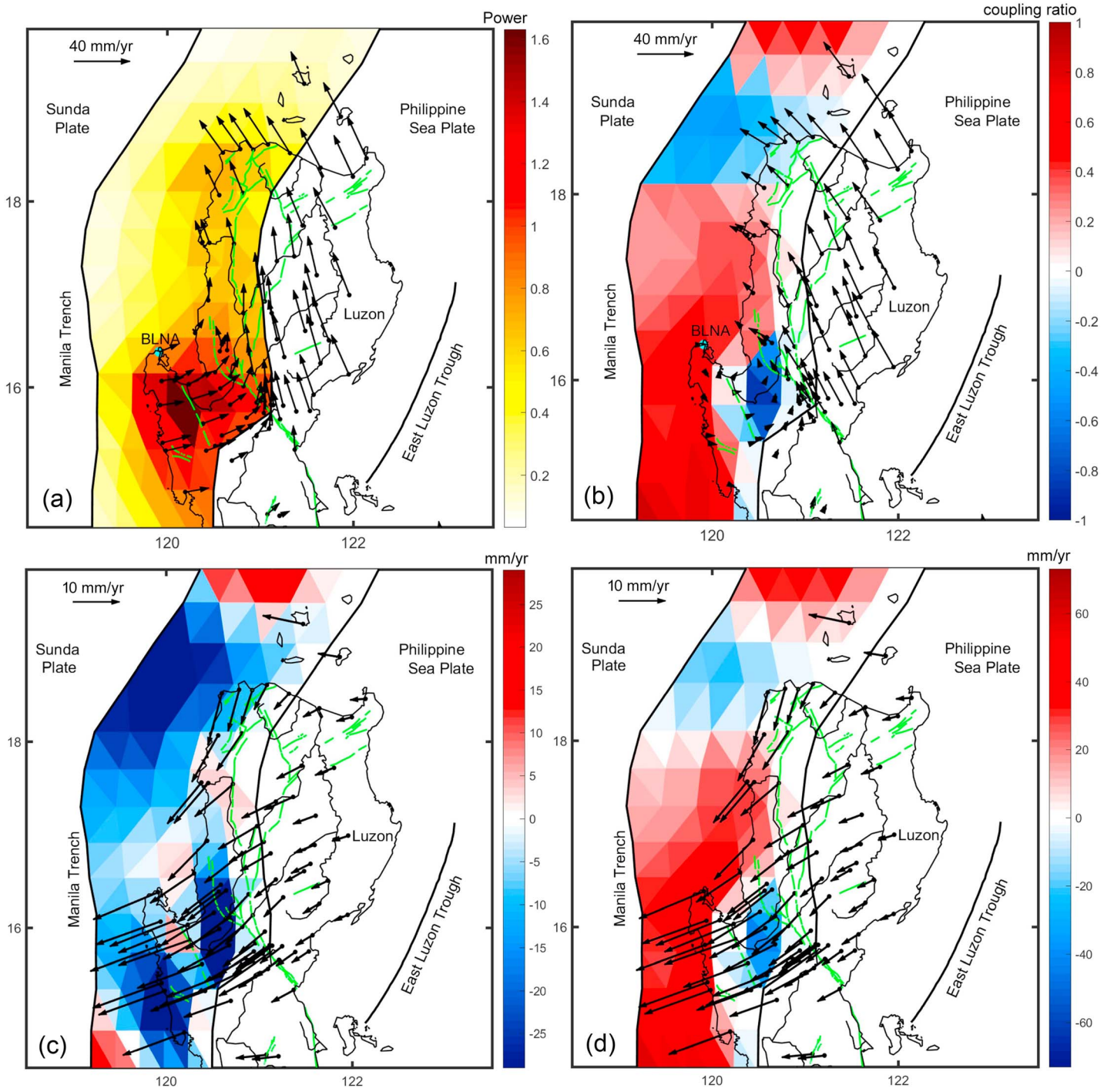

Figure 6. Power of GPS stations to constrain slip behavior, plate coupling, and slip-deficit rates in model A. (a) Power is computed by summing the magnitude of the partial derivatives that relate unit slip on the triangular elements to the displacement at the surface. The color of the triangle represents the resolving power. The black vectors show the GPS velocities with respect to BLNA site (blue dot) after subtracting elastic strain on the Manila subduction zone. (b) Coupling is defined as slip-deficit rate normalized by long-term slip rate. The black vectors show the GPS velocities with respect to BLNA site (blue dot). (c) Left-lateral and right-lateral slip-deficit rates are shown as red and blue, respectively. The black vectors are the GPS velocities due to elastic strain accumulation along the Manila Trench. (d) Reverse and normal slip-deficit rates are shown as red and blue, respectively. Vectors are the same as in Figure 6c.

convergence rate derived from geodetic data. According to Kostrov's relation [*Kostrov*, 1974], the correspondence between surface strain accumulation and scalar moment accumulation can be derived using the average strain rate tensor and the moment rate tensor within a volume. If all of the strain in a volume V is seismic, the average strain rate tensor $\dot{\varepsilon}_{ij}$ can be written as

$$\dot{\varepsilon}_{ij} = \frac{1}{2\mu V}\sum_{n=1}^{N}\dot{M}_{ij}^{n} \tag{1}$$

where μ is the rigidity and $\boldsymbol{M_{ij}}$ is the ij component of the moment tensor of the $\boldsymbol{n}$th earthquake that occurs in the volume. *Ekström and England* [1989] assumed that if the deformation in a given region is simply accommodated by the relative motion of two rigid blocks, and there is no gradient in the direction parallel to the strike of the block boundary and no shear on horizontal planes, the strain rate tensor can be written as

$$\dot{\epsilon} = \frac{\boldsymbol{v}}{2\boldsymbol{Y}}\begin{bmatrix} 2\boldsymbol{n}_1\boldsymbol{u}_1 & (\boldsymbol{n}_1\boldsymbol{u}_2+\boldsymbol{n}_2\boldsymbol{u}_1) & 0 \\ (\boldsymbol{n}_1\boldsymbol{u}_2+\boldsymbol{n}_2\boldsymbol{u}_1) & 2\boldsymbol{n}_2\boldsymbol{u}_2 & 0 \\ 0 & 0 & -2(\boldsymbol{n}_1\boldsymbol{u}_1+\boldsymbol{n}_2\boldsymbol{u}_2) \end{bmatrix} \tag{2}$$

where Y is the width of the deformation zone in the direction of $\boldsymbol{n}$; $\boldsymbol{n}$ is the unit vector normal to the boundary; 1, 2, and 3 correspond to east, north, and up, respectively; $\boldsymbol{v}$ is the relative velocity between two blocks; and $\boldsymbol{u}$ is the unit vector of $\boldsymbol{v}$. Combining equations (1) and (2), the moment rate tensor is

$$\dot{\boldsymbol{M}} = \boldsymbol{\mu XZ}\,\boldsymbol{v}\begin{bmatrix} 2\boldsymbol{n}_1\boldsymbol{u}_1 & (\boldsymbol{n}_1\boldsymbol{u}_2+\boldsymbol{n}_2\boldsymbol{u}_1) & 0 \\ (\boldsymbol{n}_1\boldsymbol{u}_2+\boldsymbol{n}_2\boldsymbol{u}_1) & 2\boldsymbol{n}_2\boldsymbol{u}_2 & 0 \\ 0 & 0 & -2(\boldsymbol{n}_1\boldsymbol{u}_1+\boldsymbol{n}_2\boldsymbol{u}_2) \end{bmatrix} \tag{3}$$

where X is the length of deforming block perpendicular to $\boldsymbol{n}$ and Z (the thickness of seismogenic zone). Assuming that μ is equivalent to 30 GPa and values of X and Z can be determined from the distribution of seismicity, we can solve for the speed and azimuth of the relative velocity between two block and the azimuth of the deforming boundary by rotating equation (3) into the coordinate frame in that minimizes the difference between the four horizontal components of the observed seismic moment rate tensor and those in equation (3). Due to the ambiguity arising from $\boldsymbol{n}$ and $\boldsymbol{u}$ being interchangeable in equation (3) [*Ekström and England*, 1989], $\boldsymbol{n}$ is specified with an angle of ±30° to the normal direction of the Manila Trench and $\boldsymbol{u}$ ranges from 0° to 360° with an interval of 2°. The amplitude of the relative velocity, $\boldsymbol{v}$, is solved from using the ratio between the scalar moment rate (the summation of earthquake scalar moments in the specified region dividing by the time interval of the catalogue) and the product of $\boldsymbol{\mu XZ}$.

5. Results

5.1. Block Modeling

We propose two plate coupling models (models *A* and *B*) in this study. Model *A*, composed of 9 blocks, produces a mean residual velocity of 3.1 mm/yr at 116 GPS stations (including 13 IGS sites), in line with the average data uncertainty of 2.3 mm/yr (Figure 5). Orientations of residual velocities are randomly distributed, suggesting that the misfit is primary associated with errors of GPS observations or local heterogeneities in deformation (Figure 5b). Estimated Euler poles of the tectonic blocks and slip-deficit rates on faults in Luzon are listed in Tables 2 and 3, respectively. Predicted velocities due only to rigid block rotations in two models are shown in Figure S7. The four E-W transects of predicted velocities are shown in Figure 4a.

Here we describe estimated slip rates on the plate boundary faults in model *A*. Spatially variable slip deficit is only allowed along the Manila subduction zone (Figure 6); all other fault segments are assumed to be fully coupled, with slip-deficit rate equivalent to the magnitude of estimated slip rate. On the Manila Trench, inferred slip-deficit vectors are roughly aligned with the long-term slip vectors (Figure S8). Model *A* shows dominantly right-lateral slip of 10–30 mm/yr except for a few fault patches with left-lateral slip of 15 mm/yr on the northern and southern ends of the Manila Trench (Figure 6c). The dip-slip deficit rates show a normal motion of 20 mm/yr at latitudes 18–19°N and 16°N (Figure 6d). These areas slipping faster than the plate convergence rate may be characterized by long-term aseismic transient events spanning the entire GPS time series, although we did not find evidence for shorter-term slow slip events in the GPS time series. When aseismic transients lasting in a long time period they may appear in GPS position time series as a reduced slope

Table 2. Estimated Euler Poles and Uncertainties of the Tectonic Blocks in ITRF2008 Reference Frame[a]

Model *A*	PSP	LARC	EPF	CC	BGT	ILOC	FARC	SP	
Longitude (deg)	340.729	113.395	94.435	118.543	299.604	121.298	121.479	265.800	
	(1.890)	(0.198)	(38.284)	(0.682)	(0.755)	(1.217)	(0.088)	(0.005)	
Latitude	−56.658	3.550	−17.936	10.657	−25.507	−18.353	4.666	48.891	
(deg)	(2.262)	(0.419)	(38.631)	(2.017)	(4.920)	(47.687)	(0.366)	(0.024)	
Rotation rate	0.691	1.848	0.637	3.414	2.758	0.857	1.898	0.335	
(°/Myr)	(0.031)	(0.042)	(0.641)	(0.944)	(1.495)	(0.965)	(0.044)	(0.000)	
Model *B*	PSP	LARC	EPF	CC	BGT	ILOC	NFARC	SFARC	SP
Longitude	340.186	106.470	120.235	119.113	250.192	114.744	300.725	120.599	248.905
(deg)	(1.791)	(0.671)	(0.429)	(0.380)	(6637.458)	(8.792)	(0.055)	(0.042)	(1.194)
Latitude	−56.030	−9.224	10.699	12.137	−88.831	−22.831	−25.430	11.385	50.640
(deg)	(2.224)	(1.308)	(0.512)	(1.158)	(110.408)	(51.233)	(0.122)	(0.206)	(0.805)
Rotation rate	0.694	1.062	5.735	5.422	0.473	0.866	9.367	4.915	0.268
(°/Myr)	(0.031)	(0.040)	(0.875)	(1.104)	(0.449)	(0.900)	(0.315)	(0.280)	(0.003)

[a]The numbers in the parenthesis show 1 standard deviation for the locations of the Euler pole and rotation rates in models *A* and *B*.

(velocity), which may be difficult to distinguish from the signature of partial coupling [e.g., *Meade and Loveless*, 2009b]. Abundant normal-faulting events near the trench axis at latitudes 18–20°N (Figure 2b) may be associated with aseismic subduction resulting in extension near trench axis [*Hsu et al*., 2012]. The sharp spatial variation of slip sense at latitudes 18–19°N and 16°N likely arises from the change of slab dip [*Bautista et al*., 2001] and the complex slab geometry used in this study (Figures S3 and S4). We also find that the total amplitude of the long-term slip rates decreases southward from 89 mm/yr at latitude 19°N to 78 mm/yr at latitude 15°N along the Manila Trench (Figure 7bc).

Model *B* (Tables 2 and 3) is composed of 10 blocks with a mean residual velocity of 3.3 mm/yr (Figure 8a) and indicated a good alignment between the rake of slip-deficit rate and the long-term motion (Figure S9). The only difference between models *A* and *B* is that model *B* includes the NLTF, segmenting the Manila Trench, which results in thrust-sense slip deficit of 30–60 mm/yr on the Manila subduction zone (Figure 8d). Model *B* shows a strong spatial variation of strike-slip deficit rates on the plate interface: 10~35 mm/yr of right-lateral slip at latitudes 16–19°N near trench axis and 10 mm/yr of left-lateral at latitudes 16–18°N on the bottom of plate interface fault (Figure 8c).

Along the East Luzon Trough, inferred right-lateral and reverse slip rates are 6.9 ± 1.7–9.9 ± 1.7 mm/yr (Figures 7b and 9a) and 0.2 ± 1.3–6.7 ± 1.2 mm/yr (Figures 7c and 9b), respectively. We notice that slip magnitudes may not be well constrained due to the sparsity of GPS sites to the east of the East Luzon Trough on the Philippine Sea Plate. Some moderate earthquakes occurred over the past decades, suggesting that this structure is active (Figure 2b).

The Philippine Fault accommodates trench-parallel motion of SP-PSP convergence and is capable of producing large earthquakes. Estimated left-lateral slip rates on the Philippine Fault system increase southward and westward. Left-lateral slip rates from north to south and east to west are 8.8 ± 1.2–9.2 ± 1.1 mm/yr on the Dalton Fault, 7.7 ± 2.1–18.9 ± 2.0 mm/yr on the Abra River Fault, and 23.3 ± 0.5–31.4 ± 1.7 mm/yr on the Digdig Fault (Figures 7b and 9a and Table 3). The Tubao Fault is characterized by right-lateral slip of 2.5 ± 2.8–10.5 ± 3.0 mm/yr. The abrupt variation in the sign of strike slip on the Tubao Fault may be influenced by the change of slab dip at latitudes 15–16°N (Figure S3). Estimated strike-slip deficit rates on the plate interface show strong spatial variation in the same region as well (Figures 6c and 8c) that may in fact reflect the complex slab geometry at this latitude. In addition, we calculate tensile motion along the vertically dipping Philippine Fault system. The Dalton Fault exhibits an opening motion of 1–9 mm/yr, whereas the Tubao Fault and most segments of the Abra River Fault are characterized by shortening, with rates of 4–14 mm/yr (Figures 7d and 9c and Table 3). We find a shortening of 6–17 mm/yr on the Digdig Fault. Inferred opening on the Dalton Fault might be related to the volcanic activity of the Central Cordillera [*Balce et al*., 1980], which is bounded to the east and to the west by the Dalton Fault and Abra River Fault, respectively. Note that the opening rate on the Dalton Fault is large despite all our efforts to put a tight constraint to reduce opening rate and test different fault geometries. Inferred shortening on

Table 3. Estimates of Slip-Deficit Rates and Uncertainties from Models *A* and *B* on Faults in Luzon[a]

Model *A*	Dip (deg)	Depth (km)	Strike Slip (mm/yr)	Dip Slip (mm/yr)	Tensile Slip (mm/yr)
Vigan-Aggao Fault	60	20	−0.1 ± 2.1	6.4 ± 3.9	
Northern Cordillera Fault (NCF)	90	20	10.5 ± 1.6		2.3 ± 2.3
Dalton Fault	90	20	9.1 ± 1.1		−7.5 ± 2.7
			9.2 ± 1.1		−9.1 ± 3.2
Abra River Fault	90	20	17.0 ± 2.2		−0.1 ± 3.4
			16.2 ± 1.9		5.9 ± 3.4
			17.3 ± 2.1		3.7 ± 3.4
			14.9 ± 2.0		11.0 ± 3.9
			18.9 ± 2.0		9.9 ± 4.0
Tubao Fault	90	20	1.9 ± 3.0		11.1 ± 4.1
			−3.7 ± 3.2		9.7 ± 4.6
			−2.5 ± 2.8		7.5 ± 4.9
			−4.8 ± 4.1		6.6 ± 5.6
Digdig Fault (DDF)	90	20	31.4 ± 1.7		11.8 ± 2.6
			30.1 ± 1.8		17.2 ± 3.0
			24.6 ± 0.4		15.4 ± 0.5
			24.6 ± 0.4		15.4 ± 0.5
East Luzon Trough	40	30	−9.9 ± 1.7	6.7 ± 1.2	
Model *B*	Dip (deg)	Depth (km)	Strike slip (mm/yr)	Dip slip (mm/yr)	Tensile slip (mm/yr)
North Luzon Trough Fault (NLTF)	90	20	24.6 ± 1.5		−30.4 ± 2.5
			31.8 ± 1.9		−40.0 ± 2.2
Vigan-Aggao Fault	60	20	8.6 ± 2.2	4.0 ± 3.4	
Northern Cordillera Fault (NCF)	90	20	3.5 ± 1.4		12.1 ± 1.7
Dalton Fault	90	20	8.8 ± 1.2		−0.9 ± 2.0
			8.9 ± 1.1		−5.4 ± 2.8
Abra River Fault	90	20	7.6 ± 2.2		−5.4 ± 1.7
			8.4 ± 2.1		−1.2 ± 1.2
			8.1 ± 2.2		0.0 ± 2.0
			7.1 ± 2.1		6.4 ± 1.3
			17.6 ± 2.0		4.9 ± 3.8
Tubao Fault	90	20	−2.8 ± 3.1		15.0 ± 3.5
			−5.5 ± 3.0		13.9 ± 3.9
			−10.5 ± 3.0		10.2 ± 4.2
			−8.6 ± 2.9		11.5 ± 4.7
Digdig Fault (DDF)	90	20	29.1 ± 1.6		7.0 ± 2.6
			28.3 ± 1.7		10.3 ± 2.9
			24.3 ± 0.5		8.9 ± 0.5
			24.3 ± 0.5		6.1 ± 0.5
East Luzon Trough	40	30	−6.9 ± 1.7	0.2 ± 1.3	

[a]Left-lateral, thrust slip rates are positive. Tensile slip rates on strike-slip faults with closing are taken as positive. Slip-deficit rates on faults with multiple segments are listed from north to south.

the Abra River Fault and Tubao Fault is possibly related to a recent E-W compression inferred from geological and structural analyses [*Ringenbach et al.*, 1990].

Here we describe slip rates on other major faults and in the western part of Luzon (Figures 7 and 9 and Table 3). The Vigan-Aggao Fault is a left-lateral wrench fault upthrust to the west, corresponding to the present-day deformation front [*Pinet and Stephan*, 1990]. We estimate dip-slip and left-lateral slip rates of 4–11 mm/yr and 0–9 mm/yr, respectively. Estimated fast reverse rates on this structure may reflect the cumulative slip on the Vigan-Aggao Fault and other offshore thrust faults [*Hayes and Lewis*, 1984] that are not considered in our model or are perhaps due to a more pronounced reverse motion at present time. On the Northern Cordillera Fault, located at the northwest termination of the Central Cordillera, we calculate left-lateral slip of 3–11 mm/yr and shortening of 2–12 mm/yr.

5.2. Moment-Deficit Rates, Fraction of Seismic Slip, and Earthquake Potential

We estimate moment accumulation rates from geodetically constrained fault slip rates obtained by our block modeling results. The moment accumulation rates along the Manila Trench from latitudes 15°N to 19°N are

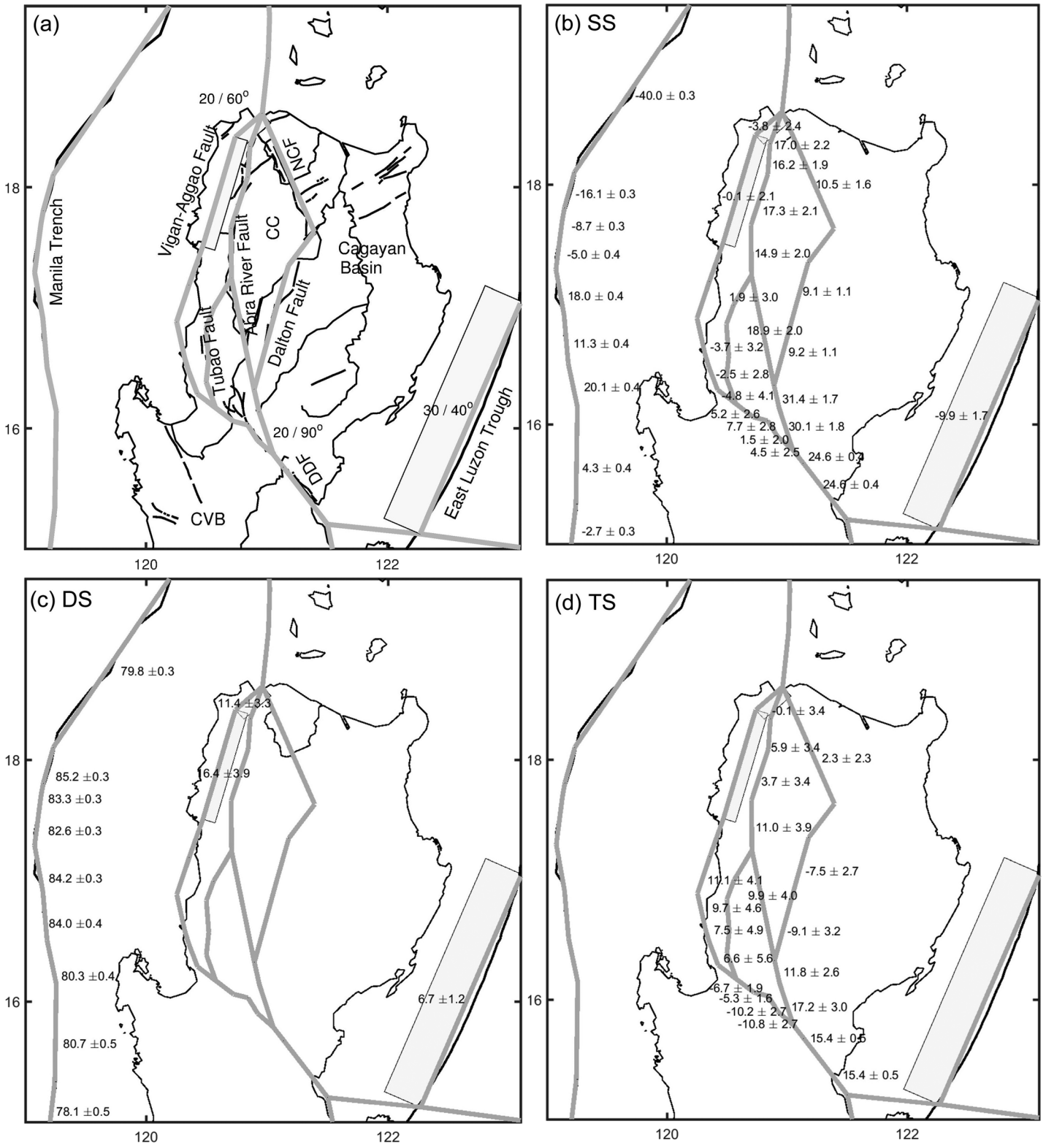

Figure 7. Fault geometry and estimated long-term slip rates in model *A*. (a) Active faults and the main physiographic provinces of Luzon. The bold gray line shows the fault surface trace. Locking depths (in km) and dip are shown in black text. The rectangle indicates the surface projection of dipping fault segments. CC: Central Cordillera; CVB: Central Valley Basin; DDF: Digdig Fault; NCF: Northern Cordillera Fault. (b) Strike-slip rates and uncertainties, in mm/yr, with left-lateral slip taken as positive. (c) Estimated dip-slip rates and uncertainties, in mm/yr, with thrust-slip taken as positive. (d) Estimated tensile slip rates, in mm/yr, on strike-slip faults with closing taken as positive.

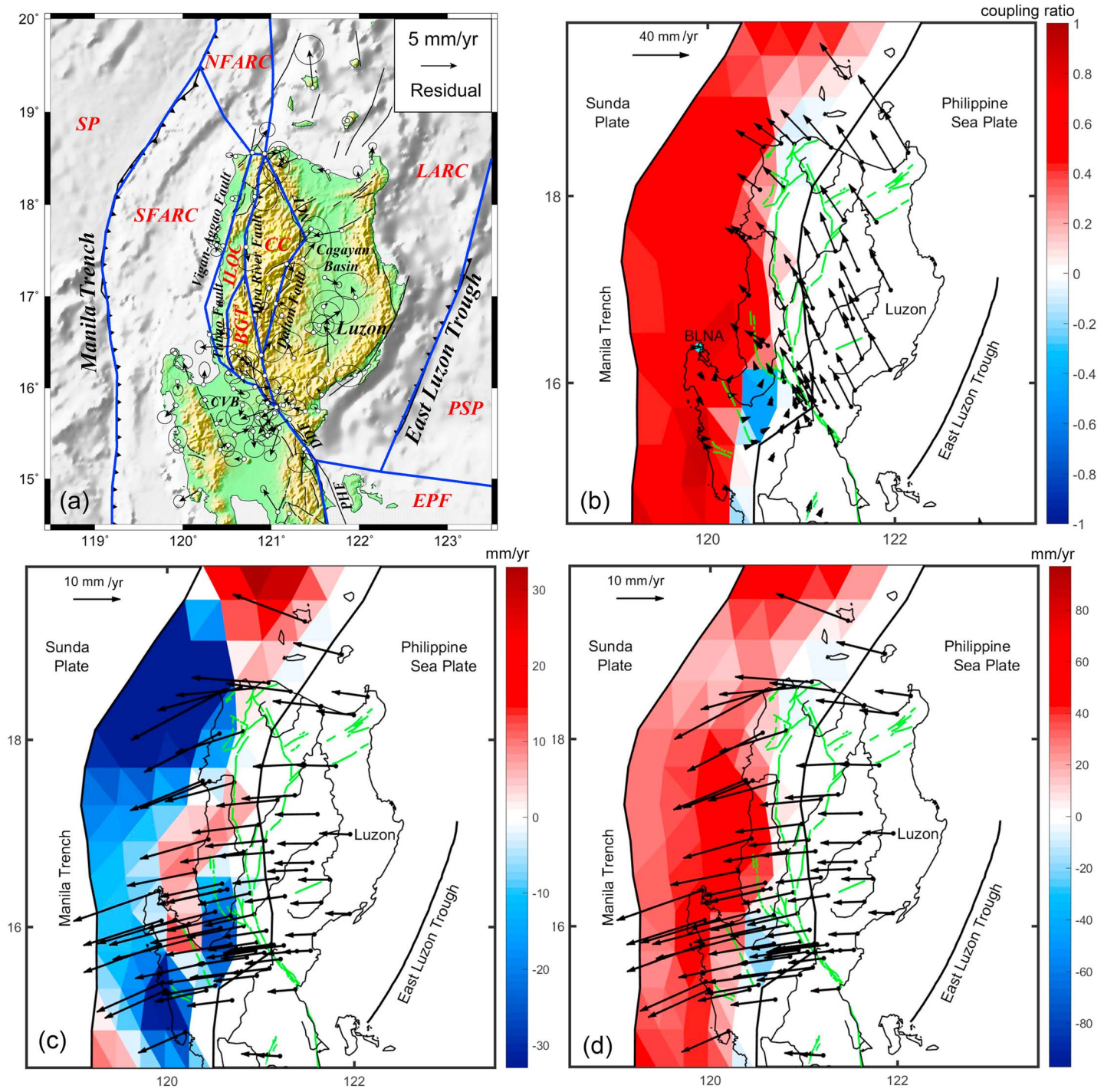

Figure 8. Residuals, plate coupling, and slip-deficit rates in model *B*. (a) Residual velocities are shown in black vectors with 67% confidence ellipses. The blue lines show the block boundaries of our preferred model. The red texts indicate the block names (Table 2). PHF: Philippine Fault; DDF: Digdig Fault; NLTF: North Luzon Trough Fault; NCF: Northern Cordillera Fault; CVB: Central Valley Basin; CC: Central Cordillera. (b) Coupling is color coded. The black vectors show the GPS velocities with respect to BLNA site (blue dot) (c) Left-lateral and right-lateral slip-deficit rates are shown as red and blue, respectively. The black vectors are the GPS velocities due to elastic strain accumulation along the Manila Trench. (d) Reverse and normal slip-deficit rates are shown as red and blue, respectively. Vectors are the same as in Figure 8c.

4.4×10^{19} N and 8.6×10^{19} m/yr, respectively, in models *A* and *B* based on a shear modulus of 30 GPa. Assuming that a future earthquake ruptures this entire section with recurrence intervals of 500 or 1000 years, the maximum moment magnitudes are 8.8–9.0 or 9.0–9.2, respectively, in models *A* and *B* (Table 4). Note that we have to make assumptions about the recurrence interval due to the absence of $M > 8$ events since 1560

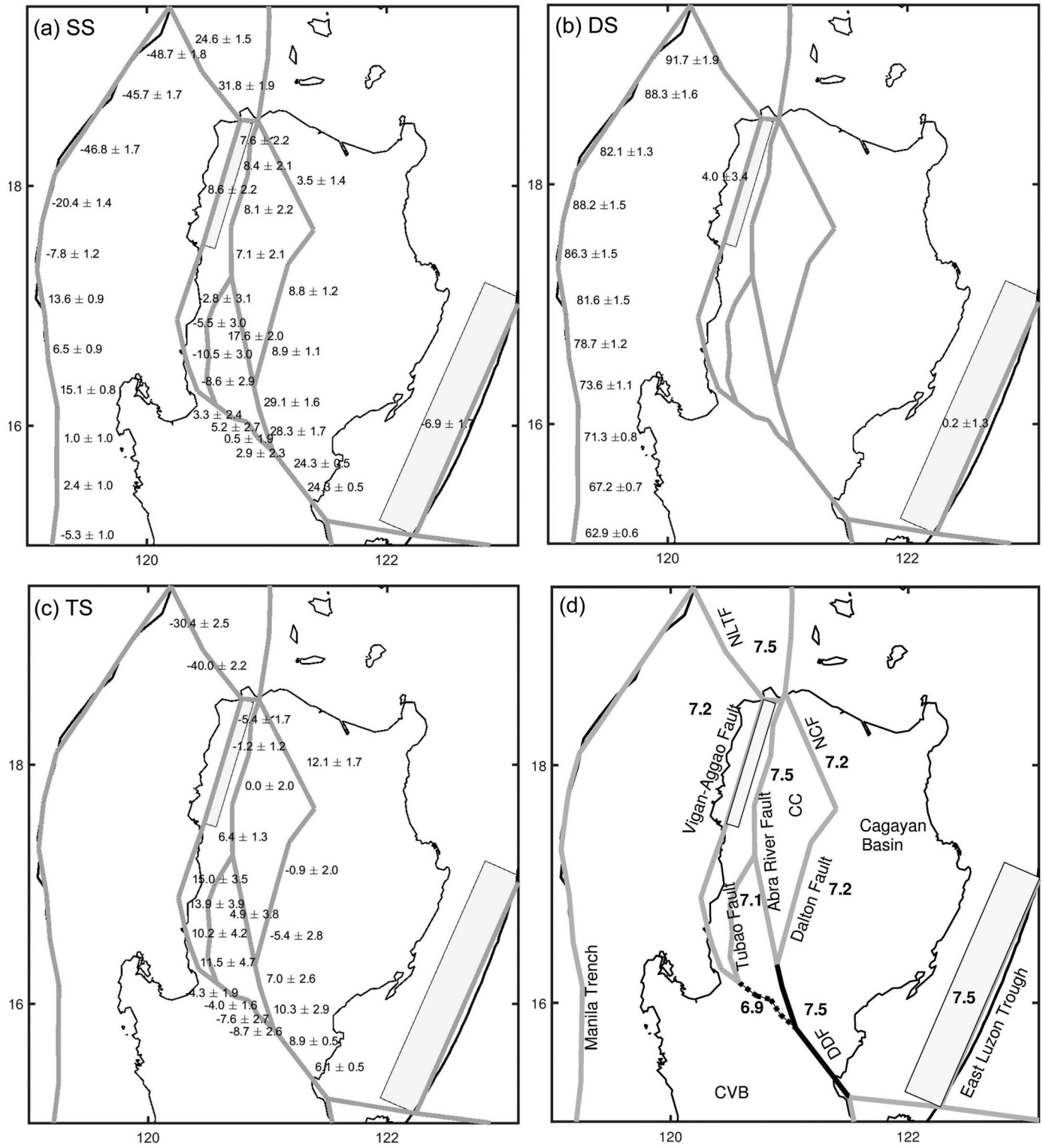

Figure 9. Estimated long-term slip rates and moment magnitudes of potential large earthquakes on faults in model *B*. Fault geometries are similar in models *A* and *B* (Figure 7a) except that model *B* includes a North Luzon Trough Fault (NLTF; see Figure 9d). (a) Strike-slip rates and uncertainties, in mm/yr, with left-lateral slip taken as positive. (b) Estimated dip-slip rates and uncertainties, in mm/yr, with thrust-slip taken as positive. (c) Estimated tensile slip rates, in mm/yr, on strike-slip faults with closing taken as positive. (d) The black text indicates the moment magnitudes of potential large earthquakes on individual fault segments given a recurrence interval of 100 years. The bold gray line shows the fault surface trace. The black line indicates the fault ruptured in the 1990 earthquake. The black dotted lines indicate the NW extension of the Philippine Fault. CC: Central Cordillera; CVB: Central Valley Basin; DDF: Digdig Fault; NCF: Northern Cordillera Fault; NLTF: North Luzon Trough Fault.

Table 4. Estimates of the Largest-Sized Earthquake from Geodetic Strain, Seismic Moment Release Rate, and Long-Term Plate Convergence in Different Areas[a]

Method Region	Geodetic (Block Modeling)	Seismic (GCMT)	GCMT + Plate Convergence Rate
Manila subduction zone (latitudes 15~19°N)	M_w 8.8~9.0 (model *A*) M_w 9.0~9.2 (model *B*) (t = 500~1000 years)	M_w 8.1~8.3 (t = 500~1000 years)	
Major faults in Luzon	M_w 6.9~7.6(model *A*) M_w 6.9~7.5(model *B*) (t = 100 years)		
The Luzon plate boundary zone	M_w 8.9~9.1(model *A*) M_w 9.1~9.3(model *B*) (t = 500~1000 years)	M_w 8.6~8.8 (t = 500~1000 years)	M_w 8.6~9(α = 0.25–0.5) (t = 500~1000 years)

[a] t: the recurrence interval and α: the fraction of seismic slip.

[*Megawati et al.*, 2009]; thereby predicted moment magnitudes may be different from current estimates when take into account uncertainties in recurrence intervals. We speculate that the subduction of Scarborough Seamount may interrupt the entire rupture of the Manila Trench. In fact, the region where we estimated creeping (18°N) is coincidentally located near the northern termination of the Scarborough Seamount (Figure 6d).

Historical earthquakes with focal depths <70 km over the past century in Luzon are shown in Figure 10a [*Engdahl and Villasenor*, 2002]. Events with magnitude greater than 7 have occurred near the Manila Trench, offshore western Luzon, East Luzon Trough, and on the Philippine Fault system. We calculate the largest-magnitude earthquakes on each rectangular segment assuming a recurrence interval of 100 years based on the frequency of $M > 7$ events (Figure 10a) and using estimates of geodetic moment accumulation rates from models *A* and *B* (Figures 7 and 9). Estimates of earthquake magnitudes are between 6.9 and 7.7 in the study area (Figures 9d and 10b). Note that these estimates that are obtained from the assumption of

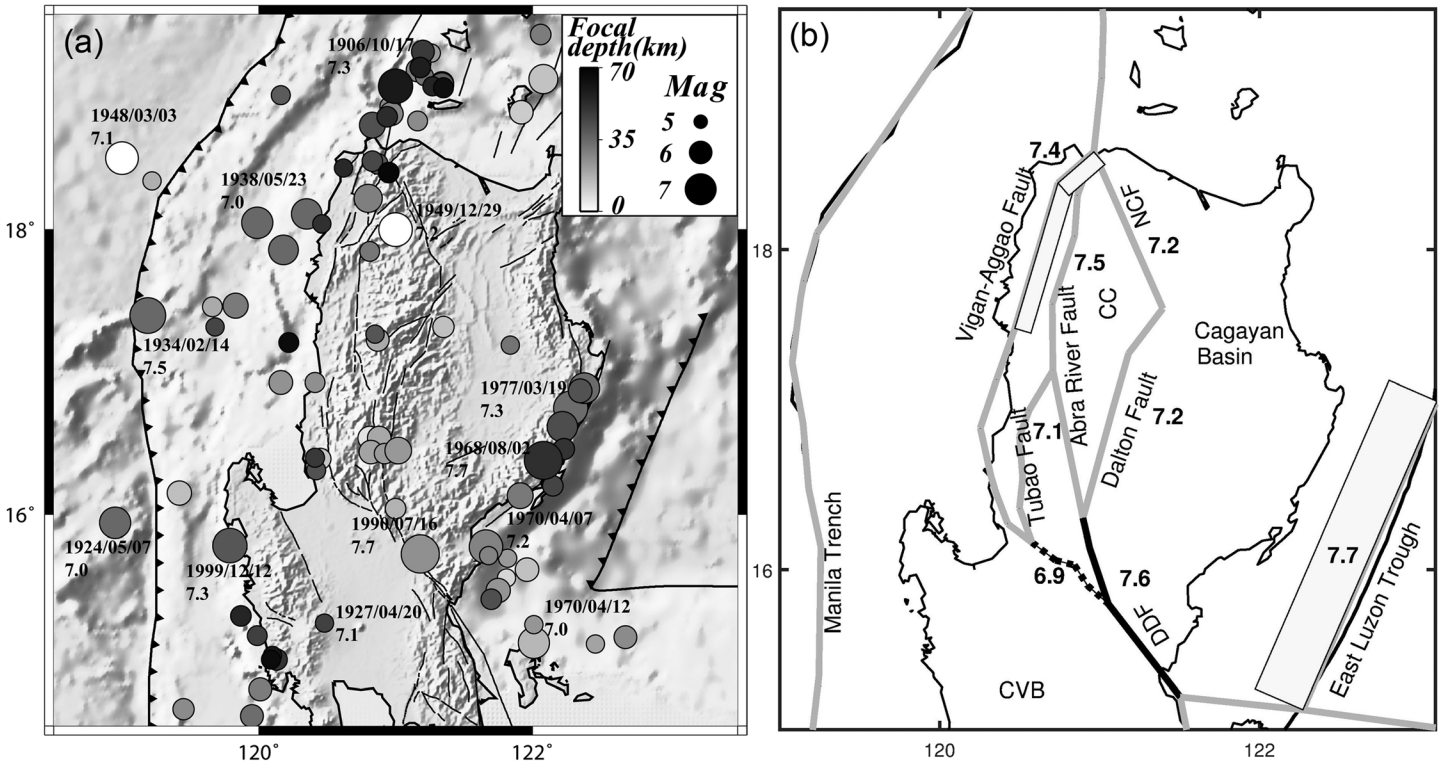

Figure 10. Seismicity (focal depth <70 km) over the past century and the moment magnitude of potential large earthquakes. (a) Seismicity from 1990 to 1999 [*Engdahl and Villasenor*, 2002]. The black text shows the date and magnitude of events. The magnitudes used here are mixing with different types (e.g., M_w, M_b, and M_s). Focal depth is color coded. The size of the circle is proportional to the earthquake magnitude. (b) The black text indicates the moment magnitudes of potential large earthquakes on individual fault segments given a recurrence interval of 100 years in model *A*. The bold gray line shows the fault surface trace. The black line indicates the fault ruptured in the 1990 earthquake. The black dotted lines indicate the NW extension of the Philippine Fault. CC: Central Cordillera; CVB: Central Valley Basin; DDF: Digdig Fault; NCF: Northern Cordillera Fault.

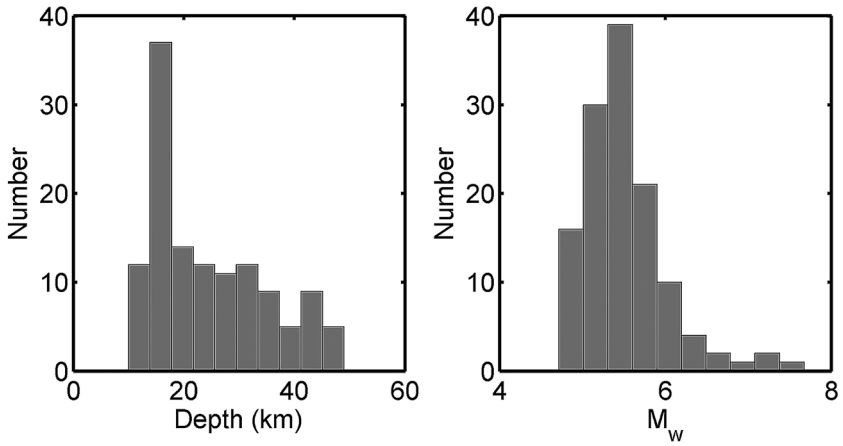

Figure 11. Distributions of (left) depths and (right) magnitudes of the GCMT earthquakes from 1976 to 2014 in the study area (Figure 2b, black box).

major faults are fully locked in Luzon and do not take into account uncertainties in recurrence intervals. The maximum size of event on the Digdig Fault is M_w 7.6, obtained by combining moments on several fault segments ruptured during the 1990 earthquake (Figures 9d and 10b, black lines). The spatial distribution of dense pockets of large historical earthquakes (Figure 10a) generally agrees with fault segments capable of generating large events (Figures 7 and 9).

Additionally, we calculate the earthquake slip vector from the sum of moment tensors using the method in section 4.2. In order to obtain a statistically meaningful estimation of the largest-magnitude earthquake, we consider a deformation zone 400 km in length and 480 km in width, similar to the size of the study area (Figure 2b, black box). About 90% of earthquakes (GCMT, 1976–2014) occur at depths shallower than 50 km, which would indicate the thickness of seismogenic zone in the Luzon plate boundary zone (Figure 11). The sum of moments and seismic moment release rate in this region are 6.9×10^{20} N m and 1.8×10^{19} N m/yr, respectively (Figure 2b, top right). Assuming recurrence interval of 500–1000 years, the slip deficit could be compensated for by earthquakes with a composite magnitude of M_w 8.6–8.8 (Table 4).

We use equation (3) to estimate the boundary normal vector of 74° and the relative motion of 30.2 mm/yr in the direction of 342° on two sides of the deforming zone (Figure 2b, top right). The long-term plate motion between the SP and PSP in this area is 86–92 mm/yr in the direction of 297° (Figure 1a), estimated using the Euler pole from our block modeling results. The slip-deficit rate inferred from the vector circuit between the long-term plate motion and the seismic slip vector suggests that a motion of 67–73 mm/yr in the direction of 280° is required to close the vector circuit (Figure 2b, top right). No great earthquakes ($M_w > 8$) have occurred at the Manila subduction zone over the past 500 years. Assuming that recurrence interval of 500–1000 years and accumulated strain is fully released by seismic slip, the maximum slip is about 34–37 and 67–73 m, respectively, which requires earthquakes with a composite magnitude of $M_w > 9$ to release the accumulated strain (Table 4). Note that this estimate is slightly larger than M_w 8.8–9.2 obtained from block modeling as the former considers accumulated strain in the entire Luzon plate boundary zone and the latter takes into account solely the accumulated strain along the subduction fault. When we calculate the sum of geodetic moments along the plate-boundary faults and major faults in Luzon, the moment accumulation rates are up to 5.8×10^{19} N m/yr in model *A* and 9.9×10^{19} N m/yr in model *B*. Given recurrence intervals of 500–1000 years, the accumulated strain could be balanced by earthquakes with a composite magnitude of M_w 8.9–9.1 in model *A* and M_w 9.1–9.3 in model *B* (Table 4), comparable with the magnitude inferred from the vector circuit. Nevertheless, estimated moment magnitudes in our study are subject to changes when using different recurrence intervals and considering aseismic processes.

To estimate the contribution of aseismic slip on the Manila subduction zone, we adopt the method that relates the geodetic moment-deficit rate to the return period of any earthquake through the Gutenberg-Richter law [*Avouac*, 2015]. This method requires the exponent *b* in the Gutenberg-Richter law [*Gutenberg and Richter*, 1944], which is calculated using the method proposed by *Stromeyer and Gruenthal* [2015].

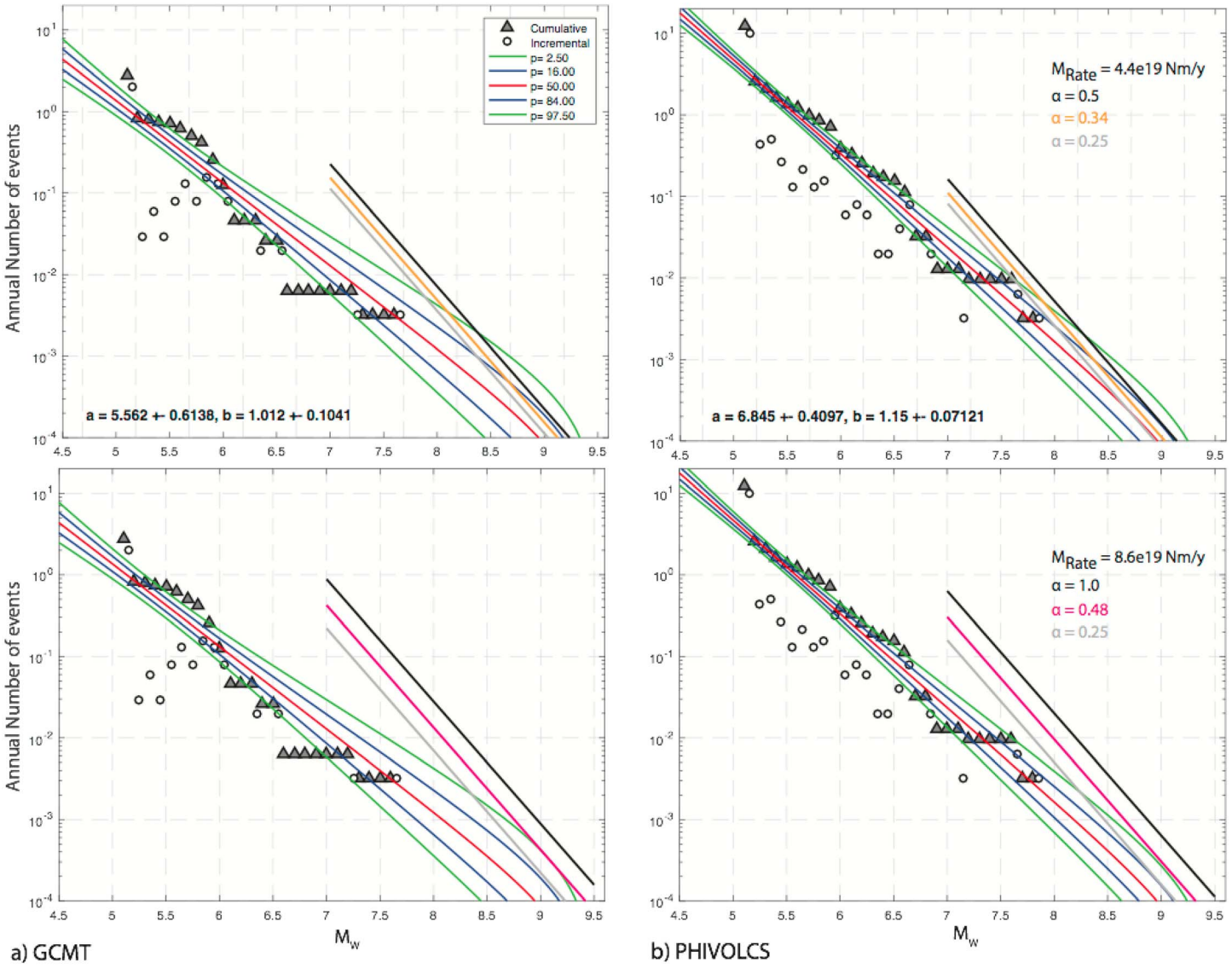

Figure 12. Magnitude frequency distributions for (a) the GCMT catalog and (b) the PHIVOLCS catalog. Incremental (circle) and cumulative (triangle) distributions of the data are shown together with the median rate model (red), together with the 16/84 percentiles (or 1 standard deviation) and the 2.5/97.5 percentiles (or 2 standard deviations). *a* value and *b* value are depicted in the bottom left of the plots. The black, orange, and gray lines on the top plots are determined by the slip budget closure condition in *Avouac* [2015] with the moment rate of 4.4×10^{19} N m/yr (model *A*) and the fraction of seismic slip of 0.5, 0.34, and 0.25, respectively. The black, magenta, and gray lines on the bottom plots are determined by the moment rate of 8.6×10^{19} N m/yr (model *B*) and the fraction of seismic slip of 1.0, 0.48, and 0.25, respectively.

Details can be found in section 6.3. For the GCMT catalog, we obtain Gutenberg-Richter parameters for the median and 1 standard deviation of $a = 5.56 \pm 0.61$ and $b = 1.01 \pm 0.10$; for the PHIVOLCS catalog, we obtain $a = 6.85 \pm 0.41$ and $b = 1.10 \pm 0.071$ (Figure 12). We use the *b* value from PHIVOLCS catalog and geodetic moment-deficit rates in models *A* and *B* and the equation (5) in *Avouac* [2015]: $\log N_{\max} = -\frac{3}{2}M_w - 9 + \log \dot{\mathscr{M}}_0 + \log\left[\alpha\left(1 - \frac{2b}{3}\right)\right]$, where $N_{\max}$ is the frequency of the maximum event, $\dot{\mathscr{M}}_0$ is the geodetic moment-deficit rate, and α is the fraction of seismic slip. By assuming various ratios of α, we obtain different straight lines and choose the lines that intersects the Gutenberg-Richer distribution at the maximum earthquake (Figure 12). These straight lines are characterized with the fraction of seismic slip of 0.25–0.5 (Figure 12b, top) and below 0.25 (Figure 12b, bottom), respectively, using the moment-deficit rates from models *A* and *B*. Taking into account the fraction of seismic slip (about 25–50% in model *A*), estimated seismic slip is 8–17 m, assuming a recurrence interval of 500 years and 17–34 m for a recurrence interval of 1000 years. In model *B*, we use the fraction of seismic slip of 0.25 and estimate seismic slip of 9–18 m based on the recurrence intervals of

500–1000 years. Note that estimates of seismic slip using model *A* based on different recurrence intervals are consistent with M_w 8.6–8.8 obtained from block modeling, although inferred seismic slip in model *B* based on recurrence intervals of 500–1000 years seem to be inconsistent with M_w of 8.8–9.0 from block modeling. The implications are discussed in section 6.3.

6. Discussion

6.1. Relative Motion Between the Sunda and Philippine Sea Plates

Prior estimates of plate convergence rates between the SP and PSP along the Manila subduction zone range from 80 to 100 mm/yr and increase southward [*Sella et al*., 2002; *Kreemer et al*., 2003]. In our model, the actual convergence rate estimated along the Manila Trench represents relative motion between the SP and a forearc block from Taiwan to Luzon (Figure 3). Our estimated plate motion of PSP relative to SP shows a gradual southward increase from 83–90 mm/yr at latitude 21°N to 88–94 mm/yr at latitude 15°N (white arrows in Figure 1a). Estimated Euler poles between SP and PSP of (65.04 ± 1.11°N, 194.19 ± 2.34°E; 0.92 ± 0.01°/Myr) in model *A* and (61.39 ± 1.10°N, 183.63 ± 1.80°E; 0.89 ± 0.01°/Myr) in model *B* are similar to those in *Sella et al*. [2002] (59.99°N, 181.24°E; 1.05°/Myr) and *Simons et al*. [2007] (58.29°N, 170.10°E; 0.91°/Myr, using the PSP pole from *Sella et al*. [2002]).

6.2. Coupling and the Largest Event Along the Manila Subduction Zone

A low plate coupling ratio of 0.34 is estimated offshore western Luzon in model *A* (Figure 6b). This finding generally agrees with estimates of plate coupling ratio in *Hsu et al*. [2012]. Nevertheless, our results provide a better spatial resolution of plate coupling due to an increase of GPS station density. We test a wide range of the strength of the smoothing constraint in section 4.1 and find that the overall distribution of plate coupling remains relatively consistent.

Using the moment-deficit rate in model *A* and the exponent *b* from PHIVOLCS catalog, we are able to plot straight lines intersecting the Gutenberg-Richer distribution at the maximum earthquake with the fraction of seismic slip of 0.25–0.5 (Figure 12b). This estimate is roughly consistent with an average coupling ratio of 0.34 in model *A*. Our alternative model *B*, which shows predominately thrust-sense slip deficit on the plate interface, produces a coupling ratio of 0.48 (Figure 8b). However, the estimated fraction of seismic slip is apparently smaller than 0.25 in model *B* (Figure 12b). The discrepancy in characterizing the seismic potential of the plate interface arising from using different methods does not mean that the inferred coupling in model *B* is incorrect. Historical seismicity in Luzon does not include $M_w > 8$ events and may not represent the seismogenic behaviors in this area over the long term. The method proposed by *Avouac* [2015] has implicit assumptions that interseismic coupling pattern is stationary; such that, the measured coupling over the past decade in Luzon can be extrapolated in the long run. In addition, the frequency-magnitude distribution from small to moderate earthquakes can be extrapolated to the seismogenic behavior of large events using the Gutenberg-Richter law. *Avouac* [2015] shows that it may be still challenging to reconcile the interseismic deformation interpreted from geodetic data with the known instrumental and historical seismicity using his method. Due to insufficient knowledge of the plate coupling along the Manila Trench, we need to consider earthquake ruptures of both scenarios viable.

We compare geodetic moment accumulation rate and seismic moment release rates along the Manila subduction zone. The geodetic estimate is 4.4×10^{19} N m/yr (model *A*) and 8.6×10^{19} N m/yr (model *B*), using slip-deficit rates on triangular fault patches of the Manila subduction fault located inside the black box shown in Figure 2b. The seismic moment release rate is 3.5×10^{18} N m/yr estimated from the sum of moments for all events located within the region covered by the Manila subduction zone projected to the surface. Note that we do not specifically select the events located at the plate interface due to the uncertainties associated with hypocentral depths in the GCMT catalog. The seismic moment release rate is approximately 4–8% of geodetic moment accumulation rate at the Manila subduction zone. The discrepancy may suggest that a portion of accumulated strain is released by aseismic events (model *A*; Figure 6b) or that the existing potential for occurrence of large earthquakes is high (model *B*; Figure 8b). We provide models to explain these two possibilities. In model *A*, aseismic deformation is implied by the relatively low coupling fractions estimated on the Manila subduction interface and a dip-slip-deficit rate faster than the plate convergence as indicated by blue triangles in Figure 6d at latitudes 17–19°N. Additionally, frequent normal-faulting events near the trench axis

Table 5. The Number of Declustered Events and Periods from GCMT and PHIVLOCS Catalogs and Parameters (*a*, *b*) in the Magnitude-Frequency Relationship Calculated Using *Stromeyer and Gruenthal* [2015]

Catalog	Period	Number of Events Declustered	Number of Events Declustered and Completely Recorded	*a*	*b*
GCMT	1976–2014	38	36	5.56 ± 0.61	1.01 ± 0.10
PHIVOLCS	1900–2015	655	110	6.85 ± 0.41	1.10 ± 0.07

(latitudes 20°N) of the northern Manila subduction zone (Figure 2b) may be related to the bending associated with the subduction of the SP and suggest that at least a portion of accumulated strain is released by aseismic slip [*Hsu et al*., 2012]. Although the GPS time series do not show evidence of short-term aseismic transients, we cannot rule out the possibility of a very long term slow slip event that spans the entire time series [*Tsang et al*., 2015; *Li et al*., 2016]. In model *B*, the plate interface is half-coupled and requires large slip events to balance the moment budget on the Manila subduction zone (Figure 8b).

6.3. Recurrence Intervals of Large Subduction Earthquakes

In section 5.2, we estimate that the upper bound of the largest subduction zone event is close to M_w 9 in the entire Luzon plate boundary zone, with a recurrence interval of 1000 years. This estimate is based on multiple simplifying assumptions because of limited knowledge in this area. The recurrence intervals for events along the subduction zone are estimated by fitting the Gutenberg-Richter model [*Gutenberg and Richter*, 1944]. We utilize a method that considers changes in completeness with time, requires predefined maximum magnitudes, and explicitly propagates the uncertainties of the Gutenberg-Richter parameters (*a* and *b* values) using their covariance matrices to the rate estimates [*Stromeyer and Gruenthal*, 2015]. This method enhances the formulations proposed previously [*Weichert*, 1980; *Johnston*, 1994; *Coppersmith et al*., 2009]. We estimate the recurrence times from two earthquake catalogs, the GCMT catalog and the PHIVOLCS earthquake record (Table 5). We choose to select the GCMT catalog as it delivers consistently determined moment magnitudes with a disadvantage of covering only the period of 1976–2014. The PHIVOLCS catalog, in contrast, offers data for the period of 1900–2014 with the disadvantage of providing a diverse set of magnitudes that need to be converted to M_w for comparison reasons.

We perform several processing steps that are detailed in Text S10. In short, we select events within a swath around the interface geometry and with time-varying completeness levels and then decluster with a window-based declustering algorithm [*Gardner* and *Knopoff*, 1974] as generally performed when modeling recurrence rates for seismic hazard assessment.

We estimate parameters of the Gutenberg-Richter relationship (*a* and *b*) following *Stromeyer and Gruenthal* [2015] for the GCMT and PHIVOLCS catalogs (Table 5) and display the results in Figure 12: median estimates (red) as well as 1 (blue) and 2 (green) standard deviations for the modeled activity rates are displayed. It is well observable that uncertainties are smallest for the magnitude range that contains the most data (5.2 to 7.0) and that large uncertainties are obtained in the regions of extrapolation, in particular for $M_w > 8.0$, i.e., for any of the largest-magnitude event on this structure. We note that uncertainties for the GCMT catalog are larger compared to the PHIVOLCS data due to the smaller data coverage. Converting these parameters to recurrence estimates, we however find results that are comparable and consistent.

The average recurrence time for an $M_w \geq 8$ event is on the order of 611 ± 300 years (PHIVOLCS) and 822 ± 700 years (GCMT), for an $M_w \geq 8.5$ event 2423 ± 2000 years and 2831 ± 3000 years (Table 6). Recurrence for $M_w \geq 9.0$ are on the order of 12,000 years, with lower bounds at a few thousand years. The seismicity records do not constrain well these recurrence times as uncertainties are on the order of the estimate itself. The seismicity-based estimates of recurrence intervals from the two different catalogs are, despite using different processing steps, in good agreement. Performing the computations without removing seismicity by a declustering algorithm indicates that recurrence times would be even larger as *b* values increase to about 0.5 without being compensated by the overall activity, thus resulting in an even more pronounced difference compared to the GPS-derived moment estimates.

The magnitude-frequency distribution using the PHIVOLCS catalog (Figure 12b) is consistent with the method proposed by *Avouac* [2015], using the moment-deficit rate from model *A* (Figure 12b, top), judging from a good alignment of modeled straight lines and the distribution of large earthquakes. However, the

Table 6. Recurrence Time in Years for Selected Magnitudes in Figure 12[a]

M_w	Recurrence Time									
	$P = 2.5\%$		$P = 16\%$		Median ($P = 50\%$)		$P = 84\%$		$P = 97.5\%$	
	GCMT	PH	GCMT	PH	GCMT	PH	GCMT	PH	GCMT	PH
8	236	255	438	393	822	611	1,532	946	2,792	1,442
8.5	671	883	1,366	1,453	2,831	2,423	5,848	4,035	11,790	6,611
9	2,380	3,714	5,263	6,491	11,907	11,528	26,909	20,464	59,327	35,709
9.3	8,119	13,806	18,720	24,856	44,250	45,539	104,579	83,429	241,011	150,166

[a]Median, 1 standard deviation (16/84 percentile), and 2 standard deviations (2.5/97.5 percentiles) are indicated. PH denotes PHIVOLCS.

result is less satisfactory when we use the moment-deficit rate from model *B* (Figure 12b, bottom). The straight lines derived from a wide range of fraction of seismic slip (0–1) do not intersect the magnitude-frequency distribution of large earthquakes. In addition, we find that geodetic moment-deficit rates derived from either models *A* or *B* cannot fit the magnitude-frequency distribution using the GCMT catalog (Figure 12 a), perhaps due to a larger uncertainty and fewer events compared to the PHIVOLCS catalog. However, the paucity of $M_w > 8$ events in Luzon may suggest that the *b* value estimated from available instrumental seismic catalogs cannot be extrapolated in the long run. Even though we find good agreement between the magnitude-frequency distribution in the PHIVOLCS catalog and the method proposed by *Avouac* [2015], it does not necessarily mean that this relationship sustains over a geologically long time horizon.

If the geodetic moment rate of 4.4×10^{19} N m/yr (model *A*) and 8.6×10^{19} N m/yr (model *B*) at latitudes 15°N to 19°N on the Manila subduction zone accumulates steadily over the average recurrence intervals of 700 and 2600 years, respectively, for $M_w \geq 8$ and ≥ 8.5 events (Table 6), the cumulative moments are equivalent to ~M_w 8.9–9.3 and ~M_w 9.1–9.5 events, respectively, using geodetic moments from models *A* and *B*. Thus, we find a discrepancy between the geodetically inferred moment accumulation rates and the recurrence intervals estimated from seismicity catalogs as indicated in previous works [*Ward*, 1998a; *Ward*, 1998b; *Meade and Hager*, 2005]. While such a discrepancy is often observed, it is unsatisfying in particular when considering that highly relevant information is likely included also in the short seismicity record of a region [*Tormann et al*., 2014; *Tormann et al*., 2015]. It may imply either missing large events in the past historical record, inaccurate estimates of complete reporting periods, and/or oversimplified assumptions in inferring slip rates from geodetic observations, including the assumption of temporal stability.

6.4. Fault Slip Rates

Our estimates of fault slip rates from a block model provide details on slip partitioning along the Philippine Fault system. The left-lateral slip rates on the major splay faults of the Philippine Fault in central Luzon (latitude ~17°N) increase westward: sinistral slip rates are 9 mm/yr on the Dalton Fault and 7–19 mm/yr on the Abra River Fault (Figures 7b and 9a). The left-lateral slip rate on the Digdig Fault is 24–31 mm/yr. Due to sparsity of GPS data, *Galgana et al*. [2007] calculated a single fault slip rate for the Philippine Fault and showed a southward increase from 17–27 mm/yr to 29–40 mm/yr. Using a two-dimensional elastic-half space dislocation model and GPS interseismic velocities from 1996 to 2008, *Yu et al*. [2013] estimated the left-lateral slip rates on the Philippine Fault to increase southward from 22 to 37 mm/yr. The sum of slip rates on all northern branches of the Philippine Fault is about 21–24 mm/yr, and the estimated slip rate is 24–31 mm/yr on the Digdig Fault in our model. These estimates are generally consistent with previous estimates of 17–27 mm/yr and 29–40 mm/yr on the northern and southern Philippine Fault [*Galgana et al*., 2007; *Yu et al*., 2013]. The overall magnitudes of slip rates are smaller in our block models because we assume that the plate boundary zone spans multiple faults rather than a single strand of the Philippine Fault alone.

On the other hand, geological and paleo-seismological investigations suggest that the slip rate on the Philippine Fault near the 1990 rupture ranges from 9 to 17 mm/yr, with an earthquake recurrence interval of about 300–400 years [*Daligdig*, 1997]. The geological slip rate is slower than our estimate of ~28 mm/yr on the Digdig Fault. A discrepancy between geologic rates and our rates is a bit more complicated, and it may suggest a temporal change in the fault slip rate, if both geologic rates and the block model results are measuring the actual slip rate on the fault. For example, the geodetically constrained slip rate may be contaminated by the postseismic deformation of the 1990 M_s 7.8 earthquake [*Beavan et al*., 2001]. In northern

Luzon, *Galgana et al*. [2007] inferred oblique sinistral-normal slip of 17–37 mm/yr on the Northern Cordillera Fault that is much larger than our estimate of 4–11 mm/yr (Figures 7b and 9a). This difference can be explained by a difference in assumed fault geometry in northern Luzon, such as our inclusion of the Abra River and Vigan-Aggao Faults, which were not considered in *Galgana et al*. [2007].

7. Conclusions

Using block models constrained by interseismic GPS velocities in Luzon, we find a southward decrease of long-term slip rates along the Manila Trench from 90–100 mm/yr at the northwestern corner of Luzon to 65–80 mm/yr near the southern termination of the Manila Trench. The geodetic moment accumulation rates are 4.4×10^{19} N m/yr in model *A* and 8.6×10^{19} N m/yr in model *B* from latitudes 15°N to 19°N along the Manila subduction zone. Model *A* shows that the subduction fault is partially locked with coupling fraction of 0.34, whereas model *B* shows a coupling ratio of 0.48 and implies that the NLTF is a major structure in the fore arc that segments the Luzon Trough. Assuming a temporally constant moment accumulation rate, rupture of the entire subduction interface would be equivalent to a M_w 9 earthquake assuming recurrence intervals of 500–1000 years. Major faults in Luzon are fully locked and capable of generating earthquakes with moment magnitudes of M_w 6.9–7.6. The observed seismic moment release rate is 3.5×10^{18} N m/yr in the Luzon plate boundary zone, approximately 4–8% of the geodetic accumulation moment along the Manila subduction zone. Using the long-term plate convergence and the seismic slip vector derived from earthquake moment tensors, the slip-deficit rate is 63–73 mm/yr in the Luzon plate boundary zone. Estimating recurrence intervals from earthquake catalogs shows increasing uncertainties with increasing earthquake magnitudes and a discrepancy between the geodetic and seismic moment releases for larger events ($M_w > 8.0$).

Acknowledgments

We thank the Editor, Jean-Philippe Avouac, and two anonymous reviewers for their thoughtful reviews and valuable comments that helped to improve the manuscript. We are grateful to many colleagues at the Institute of Earth Sciences, Academia Sinica, and the Philippine Institute of Volcanology and Seismology (PHIVOLCS) who have participated in collecting survey-mode and continuous GPS data. We are also grateful to PHIVOLCS for providing us with the earthquake catalog. The generous provision of continuous GPS data from the IGS community is also appreciated. The GPS data are available for research at http://dmc.earth.sinica.edu.tw/ based on request. GMT was used to create several figures [*Wessel and Smith*, 1998]. The *Blocks* crustal deformation modeling software is available at https://github.com/brendanjmeade/Blocks. This is the contribution of the Institute of Earth Sciences, Academia Sinica, IESAS2046, and the Ministry of Science and Technology, supported by grant AS-102-SS-A09 and MOST 102-2116-M-001-028-MY3.

References

Altamimi, Z., X. Collilieux, and L. Metivier (2011), ITRF2008: An improved solution of the International Terrestrial Reference Frame, *J. Geod*., *85*, 457–473.

Armada, L., S.-K. Hsu, C.-Y. Ku, W.-B. Doo, W.-N. Wu, C. Dimalanta, and G. Yumul Jr. (2012), Possible northward extension of the Philippine Fault Zone offshore Luzon Island (Philippines), *Mar. Geophys. Res*., *33*, 369–377.

Aurelio, M. A. (2000), Shear partitioning in the Philippines: Constraints from Philippine Fault and Global Positioning System data, *Island Arc*, *9*, 584–597.

Aurelio, M. A., J. B. Galapon, V. T. Hizon, and D. B. Sadsad (2009), Stress behavior from fault data sets within a transtensional zone, South Central Cordillera, Luzon, Philippines: Implications for mineral occurrences, *Island Arc*, *18*, 144–154.

Avouac, J.-P. (2015), From geodetic imaging of seismic and aseismic fault slip to dynamic modeling of the seismic cycle, in *Annual Review of Earth and Planetary Sciences*, vol. 43, edited by R. Jeanloz and K. H. Freeman, pp. 233–271, Annual Reviews, Palo Alto, Calif.

Balce, G. R., R. Y. Encina, A. Momongan, and E. Lara (1980), Geology of the Baguio district and its implications on the tectonic development of the Luzon Central Cordillera, *Geol. Paleontol. Southeast Asia*, *21*, 265–287.

Barrier, E., P. Huchon, and M. Aurelio (1991), Philippine Fault—A key for Philippine kinematics, *Geology*, *19*, 32–35.

Bautista, B. C., M. L. P. Bautista, K. Oike, F. T. Wu, and R. S. Punongbayan (2001), A new insight on the geometry of subducting slabs in northern Luzon, Philippines, *Tectonophysics*, *339*, 279–310.

Bautista, M. L. P. (1996), Estimation of the magnitudes and epicenters of Philippine historical earthquakes, MSc thesis, Graduate School of Science, Kyoto Univ., Kyoto, Japan.

Bautista, M. L. P., and B. C. Bautista (2004), The Philippine historical earthquake catalog: Its development, current state and future directions, *Ann. Geophys*., *47*, 379–385.

Bautista, M. L. P., and K. Oike (2000), Estimation of the magnitudes and epicenters of Philippine historical earthquakes, *Tectonophysics*, *317*, 137–169.

Beavan, J., D. Silcock, M. Hamburger, E. Ramos, C. Thibault, and R. Feir (2001), Geodetic constraints on postseismic deformation following the 1990 M_s 7.8 Luzon earthquake and implications for Luzon tectonics and Philippine Sea plate motion, *Geochem. Geophys. Geosyst*., *2*, 1015, doi:10.1029/2000GC000100.

Coppersmith, K. J., R. R. Youngs, and C. Sprecher (2009), Methodology and main results of seismic source characterization for the PEGASOS Project, Switzerland, *Swiss J. Geosci*., *102*, 91–105.

Daligdig, J. (1997), Recent faulting and paleoseismicity along the Philippine fault zone, north central Luzon, Philippines, PhD thesis, Kyoto University.

Ekström, G., and P. England (1989), Seismic strain rates in regions of distributed continental deformation, *J. Geophys. Res*., *94*, 10,231–10,257, doi:10.1029/JB094iB08p10231.

Engdahl, E. R., and A. Villasenor (2002), Global Seismicity: 1900–1999, in *International Handbook of Earthquake and Engineering Seismology, Part A*, edited by W. H. K. Lee, et al., chap. 41, pp. 665–690, Academic Press, Cambridge, Mass.

Fitch, T. J. (1972), Plate convergence, transcurrent faults, and internal deformation adjacent to Southeast Asia and the western Pacific, *J. Geophys. Res*., *77*, 4432–4460, doi:10.1029/JB077i023p04432.

Galgana, G., M. Hamburger, R. McCaffrey, E. Corpuz, and Q. Z. Chen (2007), Analysis of crustal deformation in Luzon, Philippines using geodetic observations and earthquake focal mechanisms, *Tectonophysics*, *432*, 63–87.

Gardner, J. K., and L. Knopoff (1974), Sequence of earthquakes in southern California, with aftershocks removed, poissonian, *Bull. Seismol. Soc. Am*., *64*, 1363–1367.

Gutenberg, B., and C. F. Richter (1944), Frequency of earthquakes in California, *Nature*, *34*, 184–188.

Hayes, D. E., and S. D. Lewis (1984), A geophysical study of the Manila Trench, Luzon, Philippines 1. Crustal structure, gravity, and regional tectonic evolution, *J. Geophys. Res.*, *89*, 9171–9195, doi:10.1029/JB089iB11p09171.
Herring, T. A., R. W. King, and S. C. McClusky (2002), Documentation for the GAMIT analysis software, release 10.0 ed., Massachusetts Institute of Technology, Cambridge, MA.
Hsu, Y.-J., S.-B. Yu, T.-R. A. Song, and T. Bacolcol (2012), Plate coupling along the Manila subduction zone between Taiwan and northern Luzon, *J. Asian Earth Sci.*, *51*, 98–108.
Johnston, A. C. (1994), Seismotectonic interpretations and conclusions from the stable continental region seismicity database, in *The Earthquake of Stable Continental Regions: Volume1: Assessment of Large Earthquake Potential*, edited by J. F. Schneider, pp. 4-1–4-103, Technical Report to Electric Power Research Institute TR-102261-V1, Palo Alto, Calif.
Karig, D. E. (1973), Plate convergence between the Philippines and the Ryukyu islands, *Mar. Geol.*, *14*, 153–168.
Karig, D. E. (1983), Accreted terranes in the northern part of the Philippine archipelago, *Tectonics*, *2*, 211–236, doi:10.1029/TC002i002p00211.
Kostrov, B. V. (1974), Seismic moment and energy of earthquakes and seismic flow of rocks, *Izv. Acad. Sci. USSR Phys. Solid Earth*, *1*, 23–40.
Kreemer, C., W. E. Holt, and A. J. Haines (2003), An integrated global model of present-day plate motions and plate boundary deformation, *Geophys. J. Int.*, *154*, 8–34.
Li, S. S., J. Freymueller, and R. McCaffrey (2016), Slow slip events and time-dependent variations in locking beneath Lower Cook Inlet of the Alaska-Aleutian subduction zone, *J. Geophys. Res. Solid Earth*, *121*, 1060–1079, doi:10.1002/2015JB012491.
Loveless, J. P., and B. J. Meade (2010), Geodetic imaging of plate motions, slip rates, and partitioning of deformation in Japan, *J. Geophys. Res.*, *115*, B02410, doi:10.1029/2008JB006248.
Loveless, J. P., and B. J. Meade (2011), Spatial correlation of interseismic coupling and coseismic rupture extent of the 2011 $M_w = 9.0$ Tohoku-oki earthquake, *Geophys. Res. Lett.*, *38*, L17306, doi:10.1029/2011GL048561.
Mao, A. L., C. G. A. Harrison, and T. H. Dixon (1999), Noise in GPS coordinate time series, *J. Geophys. Res.*, *104*, 2797–2816, doi:10.1029/1998JB900033.
Mathisen, M. E. (1981), Plio-Pleistocene geology of the Central Cagayan Valley, Northern Luzon, Philippines, Iowa State Univ., Retrospective Theses and Dissertations. Paper 6926.
McCaffrey, R. (2002), Crustal block rotations and plate coupling, plate boundary zones, *Geodyn. Ser.*, *30*, doi:10.1029/GD1030p0101.
Meade, B. J., and B. H. Hager (2005), Spatial localization of moment deficits in Southern California, *J. Geophys. Res.*, *110*, B04402, doi:10.1029/2004JB003331.
Meade, B. J., and J. P. Loveless (2009a), Block modeling with connected fault-network geometries and a linear elastic coupling estimator in spherical coordinates, *Bull. Seismol. Soc. Am.*, *99*, 3124–3139.
Meade, B. J., and J. P. Loveless (2009b), Predicting the geodetic signature of $M_w \geq 8$ slow slip events, *Geophys. Res. Lett.*, *36*, L01306, doi:10.1029/02008GL036364.
Megawati, K., F. Shaw, K. Sieh, Z. H. Huang, T. R. Wu, Y. N. Lin, S. K. Tan, and T. C. Pan (2009), Tsunami hazard from the subduction megathrust of the South China Sea: Part I. Source characterization and the resulting tsunami, *J. Asian Earth Sci.*, *36*, 13–20.
Minster, J. B., and T. H. Jordan (1978), Present-day plate motions, *J. Geophys. Res.*, *83*, 5331–5354, doi:10.1029/JB083iB11p05331.
Nikolaidis, R. (2002), Observation of geodetic and seismic deformation with Global Positioning System, PhD dissertation, 249 pp., Univ. of Calif., San Diego.
Pinet, N. (1990), Répartition des mouvements decrochants et chevauchements le long de frontière NW de la plaque Mer des Philippines, 316 pp, Paris.
Pinet, N., and J. F. Stephan (1990), The Philippine wrench fault system in the Ilocos Foothills, northwestern Luzon, Philippines, *Tectonophysics*, *183*, 207–224.
Rebischung, P., J. Griffiths, J. Ray, R. Schmid, X. Collilieux, and B. Garayt (2012), IGS08: The IGS realization of ITRF2008, *GPS Solut.*, *16*, 483–494.
Ringenbach, J. C., J. F. Stephan, P. Maleterre, and H. Bellon (1990), Structure and geological history of the Lepanto-Cervantes releasing bend on the Abra River fault, Luzon Central Cordillera, Philippines, *Tectonophysics*, *183*, 225–241.
Ringenbach, J. C., N. Pinet, J. F. Stephan, and J. Delteil (1993), Structural variety and tectonic evolution of strike-slip basins related to the Philippine Fault system, northern Luzon, Philippines, *Tectonics*, *12*, 187–203, doi:10.1029/92TC01968.
Sella, G. F., T. H. Dixon, and A. L. Mao (2002), REVEL: A model for Recent plate velocities from space geodesy, *J. Geophys. Res.*, *107*(B4), 2081, doi:10.1029/2000JB000033
Silcock, D. M., and J. Beavan (2001), Geodetic constrains on coseismic rupture during the 1990 M_s 7.8 Luzon, Philippines, earthquake, *Geochem. Geophys. Geosyst.*, *2*, 1016, doi:10.1029/2000GC000101.
Simons, W. J. F., et al. (2007), A decade of GPS in Southeast Asia: Resolving Sundaland motion and boundaries, *J. Geophys. Res.*, *112*, B06420, doi:10.1029/2005JB003868.
Stromeyer, D., and G. Gruenthal (2015), Capturing the uncertainty of seismic activity rates in probabilistic seismic-hazard assessments, *Bull. Seismol. Soc. Am.*, *105*, 580–589.
Tormann, T., S. Wiemer, and A. Mignan (2014), Systematic survey of high-resolution b value imaging along Californian faults: Inference on asperities, *J. Geophys. Res. Solid Earth*, *119*, 2029–2054, doi:10.1002/2013JB010867.
Tormann, T., B. Enescu, J. Woessner, and S. Wiemer (2015), Randomness of megathrust earthquakes implied by rapid stress recovery after the Japan earthquake, *Nat. Geosci.*, *8*, 152–158, doi:10.1038/NGEO2343.
Tsang, L. L. H., A. J. Meltzner, B. Philibosian, E. M. Hill, J. T. Freymueller, and K. Sieh (2015), A 15 year slow-slip event on the Sunda megathrust offshore Sumatra, *Geophys. Res. Lett.*, *42*, 6630–6638, doi:10.1002/2015GL064928.
Wallace, L. M., J. Beavan, R. McCaffrey, K. Berryman, and P. Denys (2007), Balancing the plate motion budget in the South Island, New Zealand using GPS, geological and seismological data, *Geophys. J. Int.*, *168*, 332–352.
Wang, K., and S. L. Bilek (2014), Invited review paper: Fault creep caused by subduction of rough seafloor relief, *Tectonophysics*, *610*, 1–24.
Ward, S. (1998a), On the consistency of earthquake moment rates, geological fault data, and space geodetic strain: The United States, *Geophys. J. Int.*, *134*, 172–186.
Ward, S. N. (1998b), On the consistency of earthquake moment release and space geodetic strain rates: Europe, *Geophys. J. Int.*, *135*, 1011–1018.
Weichert, D. H. (1980), Estimation of the earthquake recurrence parameters for unequal observation periods for different magnitudes, *Bull. Seismol. Soc. Am.*, *70*, 1337–1346.
Wessel, P., and W. H. F. Smith (1998), New, improved version of Generic Mapping Tools released, *Eos Trans. AGU*, *79*(47), 579, doi:10.1029/98EO00426.
Williams, S. D. P. (2003), The effect of coloured noise on the uncertainties of rates estimated from geodetic time series, *J. Geod.*, *76*, 483–494.
Wolfe, J. A. (1981), Philippine geochronology, *J. Geol. Soc Philipp.*, *35*, 1–30.

Wu, Y.-M., L. Zhao, C.-H. Chang, N.-C. Hsiao, Y.-G. Chen, and S.-K. Hsu (2009), Relocation of the 2006 Pingtung earthquake sequence and seismotectonics in southern Taiwan, *Tectonophysics*, *479*, 19–27.

Yang, T. F., T. Lee, C. H. Chen, S. N. Cheng, U. Knittel, R. S. Punongbayan, and A. R. Rasdas (1996), A double island arc between Taiwan and Luzon: Consequence of ridge subduction, *Tectonophysics*, *258*, 85–101.

Yoshida, Y., and K. Abe (1992), Source mechanism of the Luzon, Philippines earthquake of July 16, 1990, *Geophys. Res. Lett.*, *19*, 545–548, doi:10.1029/91GL02467.

Yu, S. B., L. C. Kuo, R. S. Punongbayan, and E. G. Ramos (1999), GPS observation of crustal deformation in the Taiwan-Luzon region, *Geophys. Res. Lett.*, *26*, 923–926, doi:10.1029/1999GL900148.

Yu, S. B., Y. J. Hsu, T. Bacolcol, C. C. Yang, Y. C. Tsai, and R. Solidum (2013), Present-day crustal deformation along the Philippine Fault in Luzon, Philippines, *J. Asian Earth Sci.*, *65*, 64–74.

Zhang, J., Y. Bock, H. Johnson, P. Fang, S. Williams, J. Genrich, S. Wdowinski, and J. Behr (1997), Southern California Permanent GPS Geodetic Array: Error analysis of daily position estimates and site velocities, *J. Geophys. Res.*, *102*, 18,035–18,055, doi:10.1029/97JB01380.